JGR Space Physics

RESEARCH ARTICLE
10.1029/2025JA033951

# Thermospheric Gravity Waves and Ionospheric Disturbances Triggered by Mountain Waves Over the Western US in January 2017

**Erich Becker[1], Sebastijan Mrak[2], Sharon L. Vadas[1], and J. D. Huba[3]**

[1]NorthWest Research Associates, Boulder, CO, USA, [2]Applied Physics Laboratory, Johns Hopkins University, Baltimore, MD, USA, [3]Syntek Technologies, Fairfax, VA, USA

**Key Points:**

- Mountain wave event over the western US triggers higher-order gravity waves (GWs) in the thermosphere
- Higher-order GWs have partial concentric ring structures and create ionospheric disturbances roughly consistent with GPS
- GW-resolving global modeling reveals the underlying multi-step vertical coupling mechanism

**Correspondence to:**
E. Becker,
erich.becker@nwra.com

**Citation:**
Becker, E., Mrak, S., Vadas, S. L., & Huba, J. D. (2025). Thermospheric gravity waves and ionospheric disturbances triggered by mountain waves over the western US in January 2017. *Journal of Geophysical Research: Space Physics*, *130*, e2025JA033951. https://doi.org/10.1029/2025JA033951

Received 12 MAR 2025
Accepted 20 AUG 2025

**Abstract** We analyze an episode of strong mountain wave (MW) activity over the western US from 9 to 12 January 2017 using the HIgh Altitude mechanistic General Circulation Model. We find that medium-scale MWs were generated by strong eastward flow over the Sierra Nevada and the Rocky Mountains. During this time, part of the stratospheric polar vortex jet extended from the western US to eastern Canada such that the MWs propagated into the lower mesosphere where they dissipated from westward vertical wind shear. This resulted in secondary gravity waves (GWs) that propagated into the lower thermosphere where tertiary GWs having concentric ring structures were created. With increasing altitude in the thermosphere, certain propagation directions were highlighted as a result of the dissipation induced by the tidal winds. At 260 km, we find eastward propagation during local morning over the northeastern US, equatorward propagation around local noon over the southern US, westward propagation during local afternoon over the northwestern US, and poleward propagation over Canada after local midnight. In addition, the model shows equatorward propagating larger-scale GWs over Canada from remote sources around local noon. The simulated regional GW-mean flow interaction patterns are consistent with multi-step vertical coupling triggered by the MWs. The traveling ionospheric disturbances (TIDs) during the MW event are simulated with the ionospheric model SAMI3. The simulated GWs and TIDs are consistent with the medium-to-large-scale TIDs observed over the continental US in GPS TEC data.

**Plain Language Summary** Mountain waves (MWs) result from winds blowing over mountain ridges. MWs waves are gravity waves (GWs) that propagate against the wind and appear stationary for a ground-based observer. We analyze a MW event in January 2017 when strong eastward tropospheric flow persisted for several days over the western US. This created MWs having horizontal wavelengths of several hundred km over the Sierra Nevada and the Rocky Mountains. Since the stratospheric jet stream was located over the western US during this event, the MWs propagated to the lower mesosphere where they dissipated. This triggered a dynamical process known as multi-step vertical coupling (MSVC). According to MSVC, the dissipation of GWs leads to the generation of secondary GWs that have non-zero ground-based phase speeds and propagate to higher altitudes. Upon dissipation of the secondary GWs, tertiary (higher-order) GWs are generated, and so forth. We simulate the MW event with a high-resolution whole-atmosphere model coupled to an ionospheric model. We find higher-order GWs in the thermosphere and corresponding traveling ionospheric disturbances (TIDs) that have partial concentric ring structures centered over the western US. These patterns are consistent with TIDs in the total election content observed by GPS.

## 1. Introduction

Mountain waves (MWs) are created by atmospheric flow over small and medium-scale mountain ranges. At middle to high latitudes during wintertime, and in the absence of sudden stratospheric warming events, MWs with predominantly vertical flux of westward momentum can often propagate into the stratosphere and lower mesosphere. This is because the tropospheric and stratospheric flow is predominantly eastward and this flow becomes stronger with height in the stratosphere. When medium-scale MWs (horizontal wavelengths of a few 100 km) propagate above the wind maximum around the stratopause, they become dynamically unstable and dissipate. This general behavior of medium-scale MWs during wintertime is accounted for by parameterization schemes in conventional general circulation models (GCMs) (e.g., Richter et al., 2010; McLandress et al., 2013) as well as in GCMs that resolve medium-scale MWs (Alexander et al., 2010, 2016; Sato et al., 2012; Vadas and Becker, 2019).

Even though MWs can have small scales (a few 10 km or less), which is also simulated in regional weather models with very high resolution (e.g., Hindley et al., 2020; Kruse et al., 2022), these small-scale MWs likely dissipate below the stratopause and do not contribute significantly to the poleward residual circulation in the winter mesosphere. Indeed, realistic mesospheric circulations are well simulated in GCMs that extend to the mesopause region (or higher) without taking small-scale MWs into account (e.g., Watanabe et al., 2006; Becker and Vadas, 2018). Nevertheless, for certain events, small-scale MWs can also propagate up to the mesopause region before they dissipate (e.g., Fritts et al., 2016; Lund et al., 2020).

An important effect from medium-scale MWs and other primary GWs in the winter upper mesosphere and thermosphere is related to multi-step vertical coupling (hereafter: MSVC). MSVC means that the breakdown of GW packets in the middle atmosphere is localized in space and time such that the associated momentum and energy depositions lead to imbalances in the ambient flow. According to theory (Vadas, 2013; Vadas et al., 2003, 2018; Vadas and Fritts, 2002), broad spectra of secondary GWs are excited from such imbalances. The majority of these secondary GWs have larger scales than the primary GWs, and they propagate into all horizontal directions, except for directions perpendicular to the momentum deposition from the primary GW packet. Those secondary GWs propagating against the vertical shear of the ambient flow above their generation altitude can account for significant (non-local) transport of momentum and energy to higher altitudes. The secondary GWs generated from the imbalance in the ambient flow need to be distinguished from the small-scale secondary GWs that result from the dynamic instability of an incident GW packet and represent most likely a macro-turbulent cascade with negligible non-local transport. This subject has been discussed in previous studies (e.g., Vadas et al., 2018; Becker et al., 2023, 2024). In the following we refer to secondary GWs as those GWs that are generated by imbalances in the ambient flow caused by the breakdown and dissipation of incident GW packets, giving rise to significant vertical transport of momentum and energy.

During wintertime, secondary GWs are frequently generated in the stratopause region and lower mesosphere from the dissipation of primary GWs having tropospheric origin (such as MWs) (e.g., Becker and Vadas, 2018; Vadas and Becker, 2019). Primary GWs can also be generated in the lower stratosphere by spontaneous emission (Becker, Vadas et al., 2022; Sato and Yoshiki, 2008; Vadas et al., 2023, 2024). The secondary GWs transport predominantly eastward momentum from the lower to the upper mesosphere because of westward vertical shear of the large-scale wind. The eastward secondary GWs (and the GWs from the polar vortex) dissipate in the winter mesopause region due to the strong variations of the large-scale winds associated with the semi-diurnal tide (Becker and Vadas, 2018). Since this process is again localized in space and time, tertiary GWs are generated that can propagate to higher altitudes in the winter thermosphere (Becker, Goncharenko, et al., 2022; Becker and Vadas, 2020; Vadas et al., 2024). The overall vertical coupling from the lower to the upper atmosphere via primary, secondary, and tertiary (i.e., higher-order) GWs has been dubbed MSVP (Vadas and Becker, 2019).

Recent studies about MSVC showed that GWs in the winter thermosphere during geomagnetically quiet times are primarily higher-order GWs. These GWs are often visible in the differential total electron content (hereafter: dTEC), which can be explained by the motion of ions due to collisions with the neutrals. Therefore, the observed wave perturbations in dTEC are very similar to those of the corresponding higher-order GWs when the wave propagation has a component parallel to the magnetic field. In such cases, the horizontal wavelength, period, and structure of an induced traveling ionospheric disturbance (TID) are the same as that of the GW at $z \sim 200$ km (Nicolls et al., 2014). Model results show that this mechanism can explain the daytime wave characteristics and amplitudes of quiet-time dTEC at middle latitudes during northern hemisphere winter (Becker, Goncharenko, et al., 2022; Vadas et al., 2025). Furthermore MSVC turns out to be most relevant during periods of a strong polar vortex (Becker, Goncharenko, et al., 2022; Vadas et al., 2024). Because conventional models with parameterized GWs do not simulate MSVC, the fidelity of these models is improved during periods with a weak vortex or during sudden stratospheric warming events (Harvey et al., 2022), while these models simulate even the wrong direction of the mean zonal flow in the winter polar mesosphere and lower thermosphere (MLT) when the polar vortex is strong (e.g., Becker and Vadas, 2018; Hindley et al., 2022; Noble et al., 2024; Smith, 2012). This dependence of MSVC on the polar vortex is crucial to understanding the observed correlation of daytime TIDs during geomagnetically quiet times with the strength of the polar vortex (Frissell et al., 2016; Nayak and Yiğit, 2019).

GWs in the thermosphere and wave structures in dTEC often have concentric-ring structures (e.g., Nishioka et al., 2013; Azeem et al., 2013). Vadas and Azeem (2021) analyzed such an event during late March 2015 when the thermospheric GWs causing the dTEC were high-frequency primary and secondary GWs from deep

convection over the eastern US. Convectively generated GWs associated with thunderstorms over the great plains during the warm season can often propagate directly into the thermosphere due to their long vertical wavelengths and large vertical group velocities (Vadas, 2007). Due to these characteristics it is possible that non-hydrostatic GWs having horizontal phase speeds larger than the sound speed criterion in the mesopause region (e.g., Becker and Vadas, 2020, their Section 3.2) can "tunnel" into the thermosphere (Heale et al., 2022). In addition, these primary GWs dissipate in the lower to mid thermosphere, thereby generating secondary waves. Kogure et al. (2025) presented a statistics of this vertical coupling mechanism based on weather data, satellite observations of stratospheric GWs, and ground-based Global Navigation Satellite System (GNSS) TEC observations over the continental US in 2022. They found that although the majority of concentric structures in dTEC occurred during the warm season over the great plains as expected, a number of wintertime events were observed over the northwestern US and were associated with frontal activity. As discussed by Kogure et al. (2025), cold fronts over the northwestern US during the cold season can cause convection and thereby trigger the vertical coupling mechanism discussed by (Heale et al., 2022). Such an event was investigated in greater detail in a model model study by Kogure et al. (2024). The authors found that GWs having horizontal wavelengths of about 500–700 km were generated by a southwestward propagating cold front over the western US in October 2020. These primary GWs tunneled into the thermosphere and caused TIDs. Since Kogure et al. (2024) used a hydrostatic GCM with moderate effective resolution, the simulated GW scales and GW tunneling effects may not be physically accurate.

During December to February at northern middle latitudes, however, moist convection is not a frequent generation mechanism for primary GWs. Therefore, if medium-to-large-scale partial concentric ring structures are observed in dTEC over the continental US during these winter months, it is likely that the underlying thermospheric GWs are triggered by other primary GW sources. Recently, Inchin et al. (2024) analyzed a wintertime MW event that was caused by anomalous southeastward tropospheric flow over the Rocky Mountains. These authors argued that the MWs visible in the stratospheric satellite observations would encounter critical levels in the mesopause region, which would lead to the generation of high-frequency, medium-scale GWs in the thermosphere. Thus, the paper by Inchin et al. (2024) supports the notion that concentric-ring structures of mesoscale GWs visible in dTEC during wintertime over the continental US can be secondary or higher-order GWs from MW events.

The present paper presents a case study of MSVC over the western US in January 2017, where the primary GWs were MWs generated by strong eastward flow over the Sierra Nevada and Rocky Mountains. In the next section we describe our modeling and data analysis methods that are used to investigate this MW event. Section 3 presents an overview of the temporal evolution of the event and the resulting GWs in the middle and upper atmosphere. In Section 4 we analyze the MSVC in terms of the vertical and horizontal structures of the regionally averaged momentum and energy fluxes, as well as the resulting ambient flow effects. In Section 5 we show that the simulated GWs and resulting traveling ionospheric disturbances (TIDs) are consistent with observed TIDs as deduced from GPS. Our main results are summarized in Section 6.

## 2. Models and TID Analysis

We employ the HIgh Altitude Mechanistic general Circulation Model (HIAMCM). This model is based on a standard spectral dynamical core that is extended by non-hydrostatic dynamics and thermodynamics for variable composition. It is run at a T256 spectral horizontal resolution and with 280 atmospheric layers extending up to $4 \times 10^{-9}$ hPa ($z \sim$ 400-500 km). The HIAMCM includes radiative transfer, water vapor transport and latent heating, topography, a simple slab ocean model, the full surface energy budget, and simple representations of ion drag in the thermosphere. Macro-turbulent vertical and horizontal diffusion is represented by the Smagorinsky scheme, with both diffusion coefficients depending on the local Richardson number. This diffusion scheme accommodates molecular viscosity and heat conduction in the thermosphere. Further information about these methods can be found in Becker and Vadas (2020) and Becker, Goncharenko, et al. (2022).

The HIAMCM can be nudged to the three-hourly Modern-Era Retrospective analysis for Research and Applications version 2 (MERRA-2) (Bosilovich et al., 2015; Gelaro et al., 2017). This nudging is performed in spectral space and is restricted to the large-scale flow such that the resolved GWs are not directly affected by the nudging. More specifically, we interpolate the MERRA-2 wind and temperature fields to the terrain-following grid of the HIAMCM and compute the MERRA-2 spectral representations of relative vorticity, horizontal divergence, and temperature. This allows nudging the HIAMCM in spectral space. The HIAMCM does not include

parameterization of GWs. The resolved GWs have an effective resolution corresponding to a horizontal wavelength of ~200 km. These capabilities regarding the explicit simulations of GWs and nudging to reanalysis allow for the simulation of observed events in the winter hemisphere (Becker, Vadas et al., 2022; Vadas et al., 2023). This pertains in particular to medium-scale GWs, MSVC, and the effects of higher-order GWs in the F region (e.g., Vadas et al., 2024, 2025). Our model data for January 2017 were previously used by Becker, Goncharenko, et al. (2022) and Becker and Oberheide (2023).

The SAMI3 (Sami3 is Also a Model of the Ionosphere) is a seamless, global, three-dimensional, physics-based model of the ionosphere/plasmasphere system. It is based on the SAMI2 (Huba et al., 2000). The SAMI3 simulates the temporal evolution of the plasma for seven ion species ($H^+$, $He^+$, $N^+$, $O^+$, $N_2^+$, $NO^+$, and $O_2^+$) and electrons. The temperature equation is solved for three ion species ($H^+$, $He^+$, and $O^+$) and for the electrons. Ion inertia is included in the ion momentum equation for motion along the geomagnetic field. The model uses the EUVAC model (Richards et al., 1994) for solar radiation and a dipole magnetic field in conjunction with the Richmond apex model (Richmond, 1995). The neutral composition, temperature, and winds can be specified by analytical models, empirical models, or GCMs. The electrostatic potential used in the SAMI3 in the low-latitude to midlatitude ionosphere is determined by the solution of a potential equation driven by the neutral wind dynamo (Huba et al., 2008). The potential in the high-latitude region is specified by the Weimer05 model (Weimer, 2005). A new feature of the SAMI3 is a fourth-order flux-corrected transport scheme for E × B transport perpendicular to the magnetic field. The partial donor cell method (Hain, 1987; Huba, 2003) is used, which reduces numerical diffusion and allows steeper density gradients to develop. Following Huba et al. (2023), we drive the SAMI3 with the dynamical fields winds from the HIAMCM at altitudes from 100 to 450 km. HIAMCM winds at 450 km are used to drive the SAMI3 at higher altitudes. As in Vadas et al. (2025), we analyze the simulated TEC and compare these model results with observations.

Images of TIDs are presented in Section 5. These are obtained from TEC observations based on ground-based dual-frequency GPS receivers (we use observations from the GPS constellation only). Specifically, we use publicly available data in Receiver Independent Exchange Format (RINEX) with 30s resolution over the continental US. The TEC perturbations (dTEC) are calculated as follows. We use multi-frequency observations of leveled carrier phases in geometry-free combination to derive slant TEC and then convert to vertical TEC via single-receiver bias determination and a mapping function (Mrak et al., 2021). We detrend receiver-transmitter TEC profiles by subtracting a running mean baseline implemented with the first-order Savitzky-Golay filter, which has an impulse response identical to the running-mean filter of the same length. In this study we use 30-min and 60-min filter lengths to extract medium-to-large-scale TIDs. The resulting dTEC fields are functions of the azimuth and elevation angle for each satellite-receiver pair. These observations correspond to an altitude of about 250 km, which is also the typical dissipation height of GWs reaching the F region (Vadas and Nicolls, 2012). A TID image is constructed by binning the observations to 0.15° × 0.15° horizontal boxes and smoothing with a 5° × 5° Gaussian kernel filter (Vadas and Azeem, 2021).

In addition to medium-scale TIDs (MSTIDs) and large-scale TIDs (LSTIDs) caused by GWs from MSVC, auroral heating associated with geomagnetic activity causes LSTIDs that propagate equatorward from the auroral region on the day-side (Lyons et al., 2019). Hence, during geomagnetic storms, the LSTIDs are likely a superposition of LSTIDs from MSVC and large-amplitude LSTIDs from auroral activity. We estimate the relative importance of geomagnetic activity for the TIDs observed over the continental US during the MW event. Figure 1 depicts geomagnetic conditions from 9 January (0 UT) to 14 January (0 UT) in 2017. Figure 1a shows the Interplanetary Magnetic Field, whose north-south component, $B_z$, remained weak (below 5 nT) during the MW event, suggesting at most moderate storm activity. Figure 1b shows the Planetary K-index (Kp) which also does not indicate any major geomagnetic activity since Kp ≤ 4 during the MW event. Figure 1c shows the SMR index, which is a proxy for the strength of the ring current. This index suggests a geomagnetically quiescent period. Finally, Figure 1d shows the SMU and SML auroral indices which are proxies for the strengths of the eastward and westward auroral electrojets, respectively. If we use the SML index as an indicator for substorm activity, then auroral sources of LSTIDs may have been significant during the second half of 9 and 10 January due to peaks of the SML with values $< -400$nT. It is important to keep this possibility in mind since our HIAMCM and SAMI3 simulations do not account for GWs and TIDs from geomagnetic forcing.

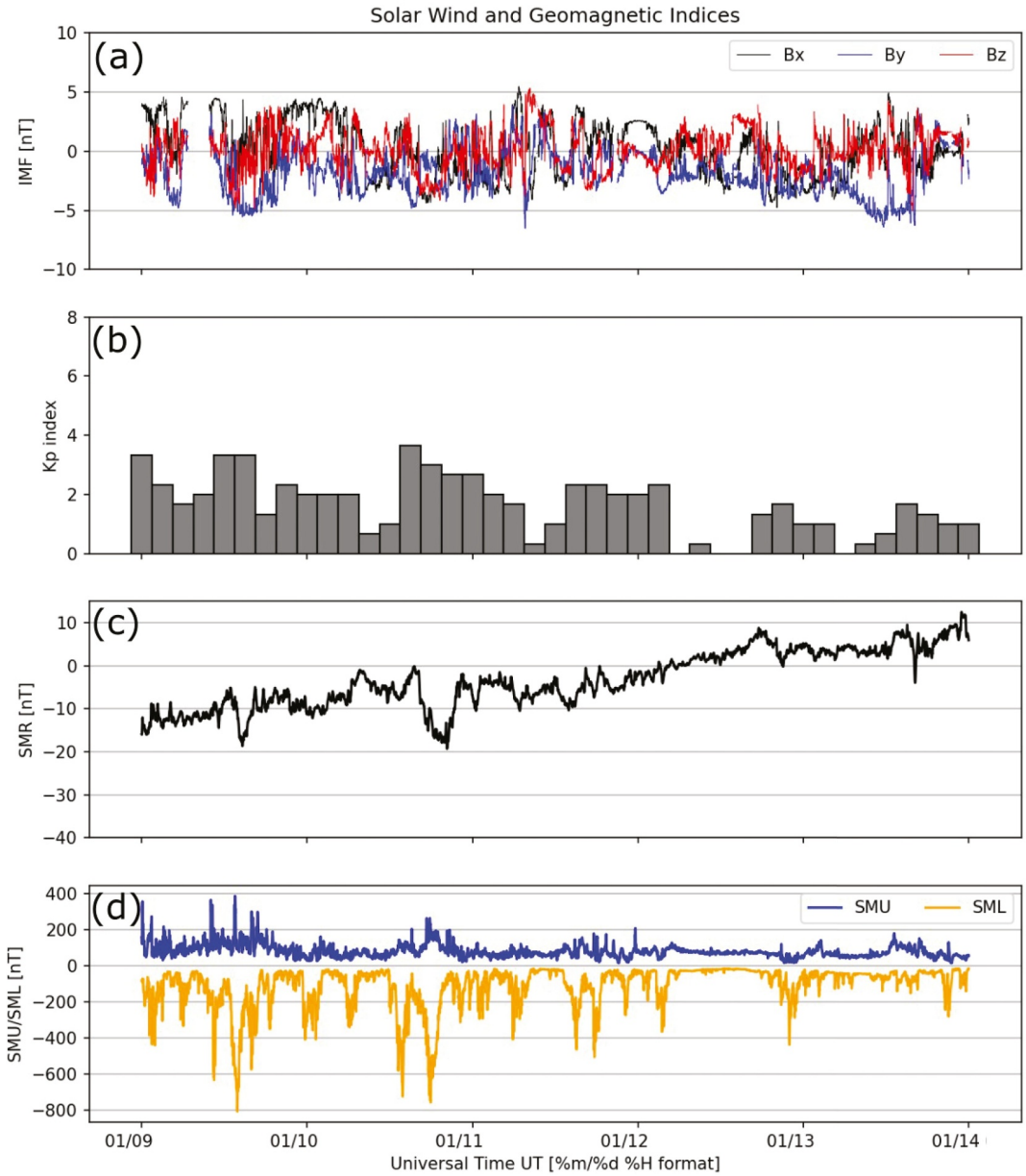


**Figure 1.** Solar wind and geomagnetic indices from 9 January (0 UT) to 14 January (0 UT) 2017. (a) Interplanetary Magnetic Field from OMNIWeb. (b)Kp index. (c) SMR index as the proxy for ring current. (d) Auroral eastward/westward electrojet indices SMU/SML. See the Data Availability Statement for source information about these indices.

## 3. Temporal Evolution of the MW Event From the Lower to the Upper Atmosphere

Figure 2a shows the orography that is used in the HIAMCM when run at a T256 horizontal resolution. Figure 2b shows the details of this orography over North America. The major mountain ridges associated with the Sierra Nevada and the Rocky Mountains are well represented. Hence, strong tropospheric flow over these mountain ridges will generate medium-scale MWs that are resolved by the HIAMCM. Figure 3 shows the large-scale flow (horizontal wavelengths larger than 1350 km) in terms of the horizontal wind speed (colors) and the horizontal streamfunction (white contours) in the troposphere (at ∼400 hPa, corresponding to $z \sim 6$ km) and upper stratosphere (at ∼1 hPa, corresponding to $z \sim 46$ km). These fields are plotted as daily averages on 10 January 2017 (upper two panels) and three days later on 13 January 2017 (lower two panels). There is strong eastward flow over the western US in the troposphere on 10 January (Figure 3a). In addition, there is a pronounced wind

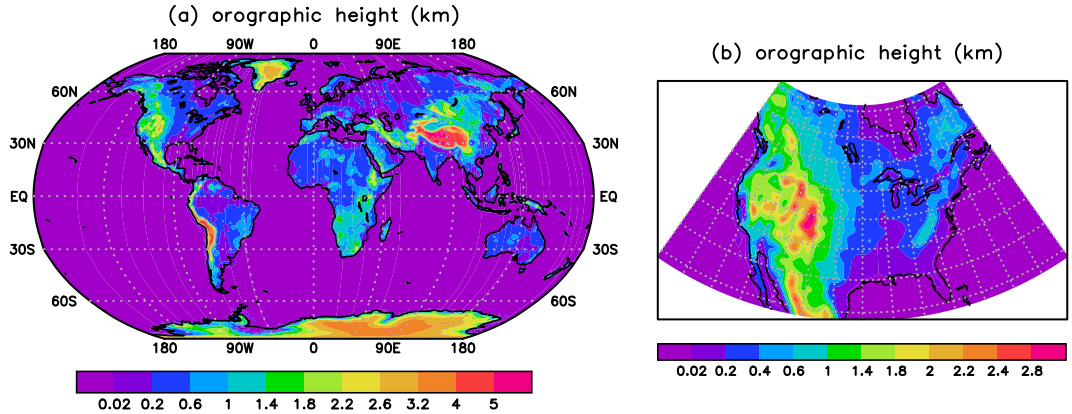


**Figure 2.** Height (km) of the orography used in the HIgh Altitude mechanistic General Circulation Model. (a) Global map. (b) Blowup over the North America from 24°N to 61°N and from 130°W to 60°W.

maximum associated with the polar vortex in the stratosphere, while the wind direction changes to northeastward with height over the US (Figure 3b). This suggests that MWs with significant amplitudes are generated during this day over the western US. Moreover, these MWs can propagate up to the stratopause region because of the eastward wind component; that is, the wind component that is opposite to the predominantly westward intrinsic propagation direction of the MWs increases with altitude and thereby Doppler-shifts the MWs to larger vertical group velocities and larger vertical wavelengths. Figures 3c and 3d show the same plots 3 days later on 13 January 2017. On this day, there is only weak tropospheric flow over the western US, and the wind maximum of the polar vortex jet has shifted eastward, extending from eastern Canada to Iceland. Hence, we do not expect significant medium-scale MWs over the western US, neither in the troposphere nor in the stratosphere.

This scenario is confirmed by Figure 4 which shows horizontal slices slices of the simulated vertical (colors) and horizontal wind (arrows) over North America from 10 January (00:00 UT) to 13 January (16:00 UT) at $z = 6$ km every 8 hr. The horizontal wind shows some cyclonic flow on 11 January over southern Canada. The vertical wind shows strong MWs over the Rocky Mountains and the Sierra Nevada throughout 10 and 11 January, as well as during the first half of 12 January. The GW activity in other regions is negligible compared to the MWs. On 13 January, the GW activity is negligible over the continental US and southern Canada. We therefore conclude that primary tropospheric GW sources other than MWs were negligible in triggering MSVC over the continental US during 10–13 January 2017. In particular, the mechanism proposed by Kogure et al. (2024, 2025) regarding events of convectively generated GWs over the western US from cold fronts during the winter months is not relevant for the MW event investigated in this study.

Figure 5 shows the temporal evolution of the GW activity over the western US in terms of the simulated vertical wind as a function of longitude and time, from 135°W to 75°W and from 9 January at 0 UT (day 8.0) to 13 January at 24 UT (day 13.0), at different heights and latitudes. Here, we measure the universal time in units of days, starting with day = 0.0 on 1 January, 00:00 UT. The large-scale zonal wind (including horizontal wavelengths $\lambda_h > 2000$ km only) is inserted with black contours. From Figure 5a we can see that the MW event starts before 9 January, and that strong tropospheric zonal flow is present from the second half of 9 January to about the end of 11 January. The MW event ceases during 12 January as a result of weakening of the zonal flow. Over the course of the MW event we observe two separate tropospheric MW packets, where one is located over the Sierra Nevada (~120°W) and another over the Rocky Mountains (~105°W). Note that MWs in the troposphere from both ridges are captured at 38°N (Figure 5a). The two MW packets spread somewhat longitudinally while propagating into the stratosphere. As a result, only one big MW packet is visible at 38°N and $z = 45$ km (Figure 5b). At this altitude, we observe a rapid weakening of the zonal flow around day 11.5 (12 January, 12 UT). According to the ray tracing equations for GWs (e.g., Senf and Achatz, 2011, their Section 3), this transient change in the background wind causes the MWs to propagate upstream, as is visible by the curved phase lines in Figure 5b.

In the upper mesosphere at $z = 85$ km and 38°N (Figure 5c), the GWs show irregular phases and variable scales. In addition, we can see strong variations of the large-scale wind. These variations are due to tides and traveling planetary waves. Since the MWs no longer exist at this altitude, they must have dissipated between the upper

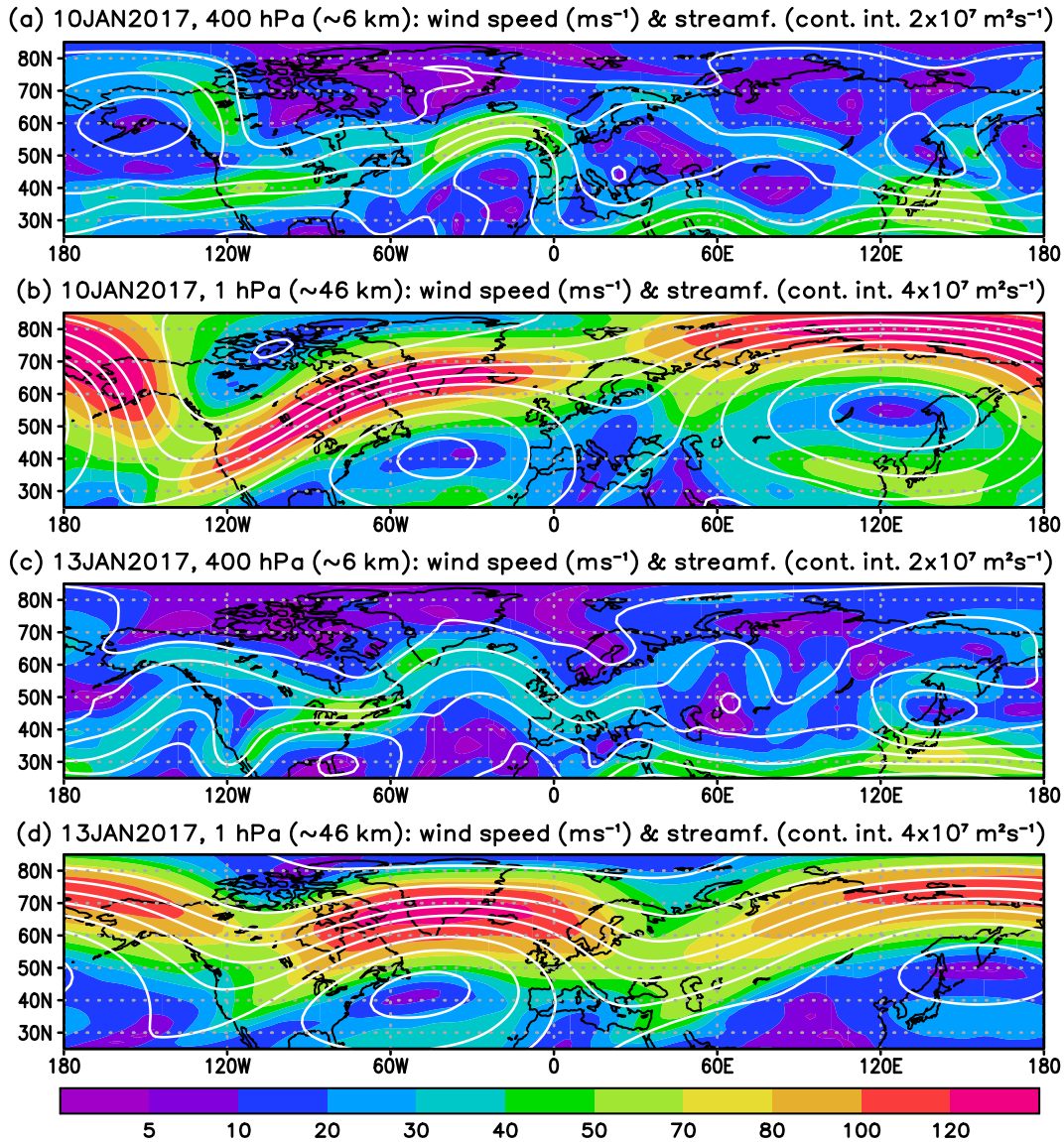


**Figure 3.** Large-scale circulation in the northern hemisphere on 10 January 2017 (a, b) and 13 January (c, d): Daily averages of the horizontal wind speed (colors) and the horizontal streamfunction (white contours). Panels (a) and (c) are at 400 hPa ($z \sim 6$ km) while panels (b) and (d) are at 1 hPa ($z \sim 46$ km). The color scale for the wind speed is the same for all panels, while the contour interval for the streamfunction at 1 hPa is twice the contour interval at 400 hPa. The large-scale flow is defined by retaining all horizontal wavelengths having $\lambda_h > 1350$ km.

stratosphere and upper mesosphere. The GW variations seen at $z = 85$ km are presumably a superposition of secondary GWs and smaller-scale GWs resulting from the forward macro-turbulent cascade induced by dynamic instability of these secondary GWs. This cascade is partly resolved by the HIAMCM (Becker, Vadas et al., 2022).

The lower row in Figure 5 shows the results at 48°N. Even though there is no MW forcing in the troposphere at this latitude over the selected time period (Figure 5d), the MWs generated around 38°N are seen in the upper stratosphere at 48°N (Figure 5e). The reason is that there was a significant southward component of the large-scale flow in the lower troposphere on 8 January that ceased around 12 UT on 9 January (day 8.5) (not shown). Hence, even though the predominant intrinsic propagation direction of the MWs was westward, they had also a significant northward component. When the southward component of the large-scale flow ceased, the MWs were swept northward and became visible at 48°N in the stratosphere. The picture in the upper mesosphere at 48°N (Figure 5f) is similar to that at 38°N, albeit showing somewhat stronger GW amplitudes. We conclude that

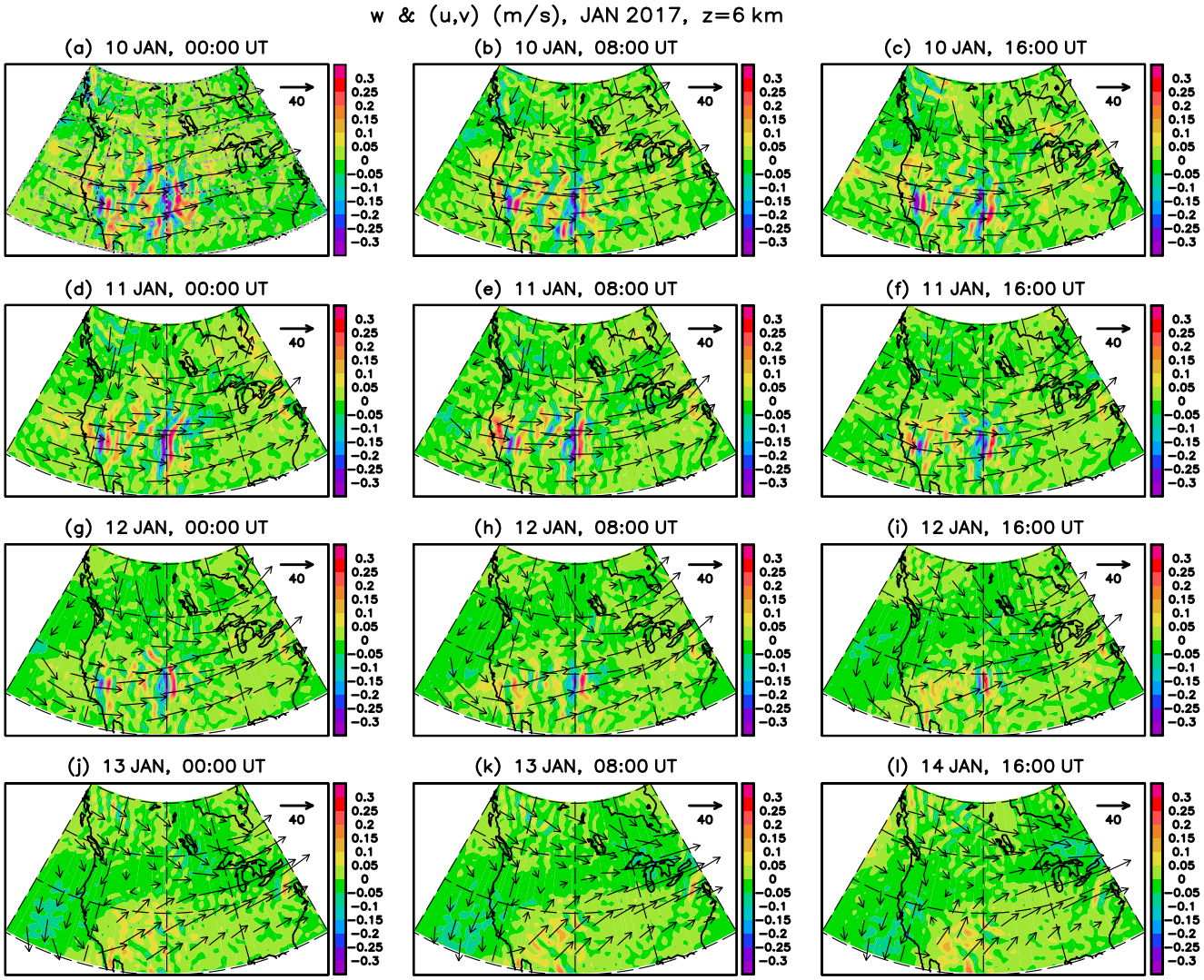


**Figure 4.** Horizontal slices over North America of the simulated vertical wind (colors) and horizontal wind (arrows) from 10 January, 00:00 UT to 13 January, 16:00 UT (2017) at $z = 6$ km with a cadence of 8 hr. These wind fields include all resolved scales. The latitude is from 30°N to 60°N (latitude circles every 10°), and the longitude is from 135°W to 75°W with meridians every 15°. The plots are centered at 105°W and 45°N (the location of the mountain wave generation over the Rocky Mountains is about 105°W and 40°N). The arrow scale for the horizontal wind is given in the upper right corner of each panel in $ms^{-1}$. Note that the color and arrow scales are the same for all panels.

secondary GW generation from MW breaking is relevant also north of the MW generation region due to the northward extension of the MWs in the stratosphere.

Figure 6 illustrates the temporal evolution of MSVC induced by the MW event in terms of horizontal snapshots at different heights (rows) and times (columns) on 11 January 2017. In the upper stratosphere at $z = 45$ km (first row), we can discern the separate MW packets from the Sierra Nevada and the Rocky Mountains. The latter extends northward to about 55°N. This is likely because the MWs were swept northward as a result of the variability of the large-scale tropospheric flow as discussed above. Note that the large-scale flow in the upper stratosphere (black arrows) hardly changes between 16 UT and 23 UT. Furthermore, the GW phases deviate significantly from being perpendicular to the large-scale wind because the wind direction changes from nearly eastward to northeastward from the troposphere to the stratosphere.

At $z = 85$ km (second row in Figure 6), the phase structures of the GWs over the western US indicate partial concentric ring structures and high temporal variability. These GWs are the secondary GWs generated as a result of the dissipation of the MWs. Note that the large-scale flow (arrows) is subject to high variability due to tides and

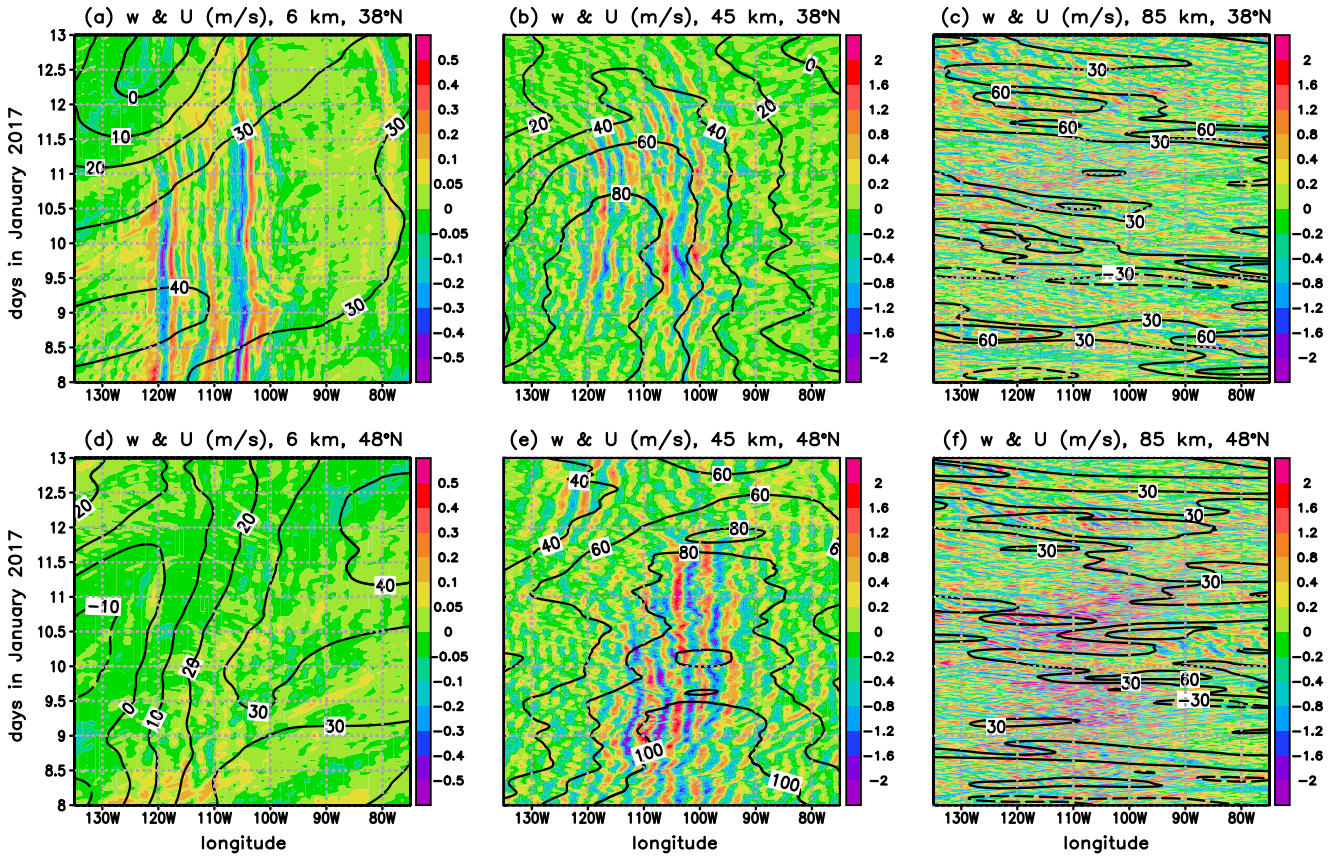


**Figure 5.** Longitude-time plots of the simulated vertical wind (colors) and the large-scale (horizontal wavelengths $\lambda_h > 2000$ km) zonal wind (contours) from 9 January 00:00 UT to 13 January 24:00 UT in 2017. The time unit is days, starting with 0 on 1 January at 00:00 UT. (a) Troposphere ($z = 6$ km) at 38°N, contour interval 10 ms$^{-1}$. (b) Stratosphere ($z = 45$ km) at 38°N, contour interval 20 ms$^{-1}$. (c) Mesosphere ($z = 85$ km) at 38°N, zonal wind contours for −30, +30, +60 ms$^{-1}$. Positive (negative) zonal winds are plotted with solid (dashed) contours. (d)–(f) Same as (a)–(c), but at 48°N.

traveling planetary waves, while the quasi-steady planetary Rossby wave structure that is predominant at $z = 45$ km is no longer visible. The GW phases look different in the lower thermosphere (third row, $z = 110$ km) than in the upper mesosphere, indicating that these GWs may be a new generation of GWs excited from the dissipation of the secondary GWs. Overall, the GW structures at $z = 110$ km are indicative of partial concentric ring structures centered over the Rocky Mountains. The large-scale background flow at this altitude is highly variably in time because of the large amplitude of the semi-diurnal tide in the lower thermosphere at wintertime middle latitudes (e.g. Becker and Oberheide, 2023, their Figure 2). The GWs, however, do not indicate dissipation induced by the tidal winds at $z = 110$ km because this altitude is close to or even lies within their generation region.

At higher altitudes in the thermosphere (fourth row in Figure 6, $z = 260$ km), the large-scale background flow is governed by the in situ generated diurnal tide. The GWs show partial concentric ring structures with large amplitudes farther away from the Rocky Mountains, for example, in the region over the eastern US. South of 50°N and over the course of 7 hr (from 16 UT to 23 UT), the predominant propagation direction of the GWs changes from eastward to southwestward. At the same time, the wind direction changes from approximately northwestward to northeastward. Hence, the predominant GWs at $z = 260$ km propagate roughly against the background tidal winds. Over Canada (north of about 50°N), we can infer higher-order GWs from other sources. These GWs have southeastward components during local morning (16 UT) and southwestward direction at local afternoon (23 UT). Further inspection of the model data showed that these GWs over Canada were higher-order GWs that had a source in the lower thermosphere over Siberia and were propagating over the pole, similar to the example discussed by Becker, Goncharenko, et al. (2022, their Figure 6) and other examples discussed in Vadas et al. (2024).

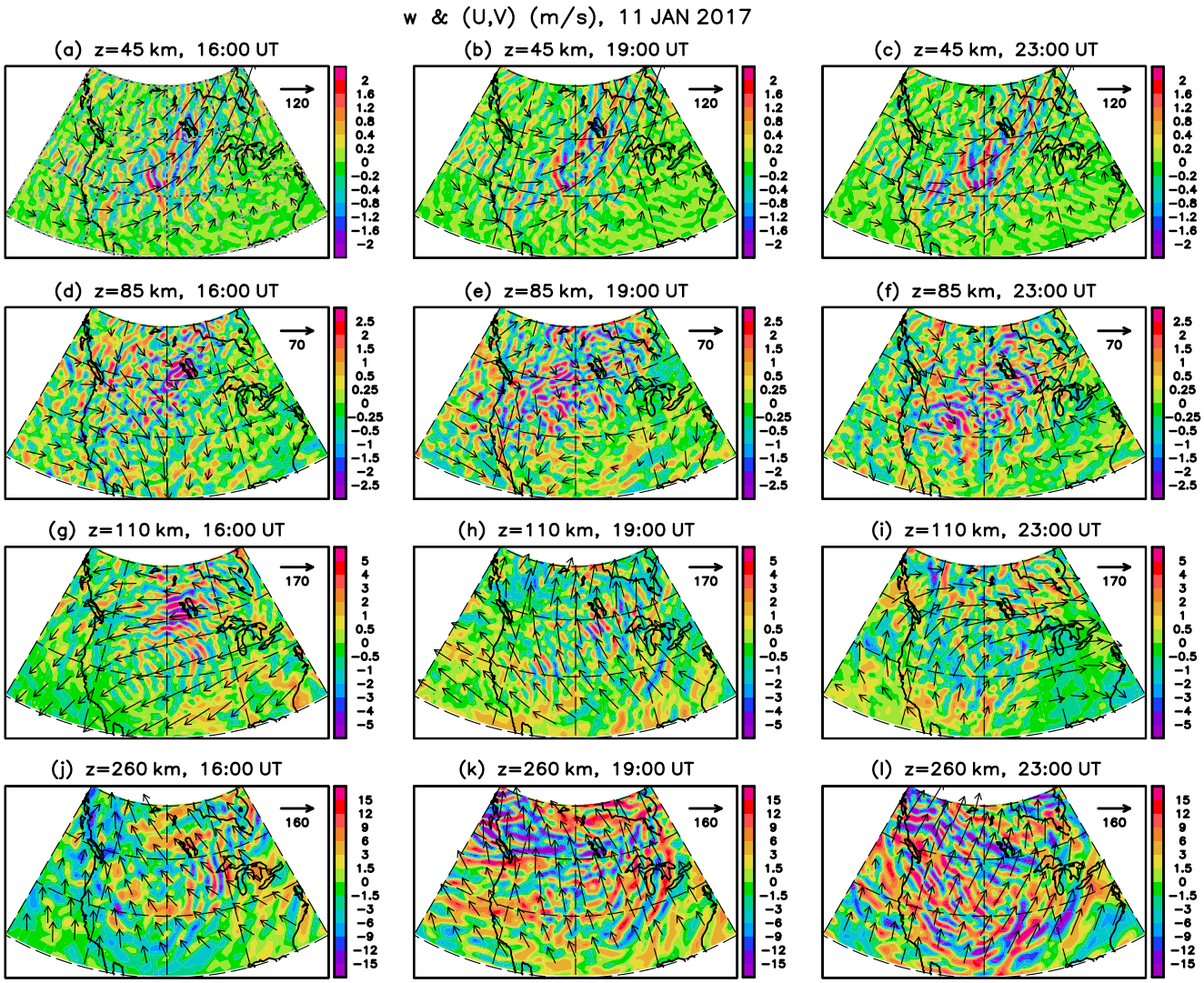


**Figure 6.** Horizontal slices over the continental US and southern Canada of the simulated vertical wind (colors) and the large-scale ($\lambda_h > 2000$ km) horizontal wind (arrows) on 11 January 2017 at different heights (rows) and different times (columns). Left, middle, and right column: 16, 19, and 23 UT. Upper to lower row: $z = 45$ km, $z = 85$ km, $z = 110$ km, and $z = 260$ km. The latitude is from 30°N to 60°N (latitude circles every 10°), and the longitude is from 135°W to 75°W with meridians every 15°. The plots are centered at 105°W and 45°N (the location of the mountain wave generation over the Rocky Mountains is about 105°W and 40°N). The arrow scale for the horizontal wind is given in the upper right corner of each panel in $ms^{-1}$. Note that the color and arrow scales differ from row to row.

The MW event over the western US lasted for several days as a result of the particular pattern of the tropospheric and stratospheric jet streams. The more common situation during wintertime is characterized by strong tropospheric flow over the eastern US and western Atlantic, as was the case on 13 January 2017. On this day, there was also a strong stratospheric vortex jet from Quebec to Scandinavia instead of over western North America (see Figures 3c and 3d). Figure 7 shows the same plots as Figure 6, but for 13 January 2017. At $z = 45$ km (upper row), there is a GW packet over western Canada. These waves are presumably MWs, but they have much weaker amplitudes than the MW packet on 11 January (note the nonlinear color scale used to plot the vertical wind). This GW packet is no longer visible at 85 km (second row in Figure 7). A more random pattern of GWs with amplitudes much smaller than on 11 January is found at this altitude. This indicates that the strong MSVC associated with the MW event from 9 to 12 January 2017 is not observed when the MWs are absent. Accordingly, no significant tertiary GW generation is visible in the lower thermosphere over the continental US and southern Canada (third row in Figure 7). At higher latitudes in the thermosphere (fourth row), we observe GWs propagating southeastward to southwestward; these GWs originate from remote sources.

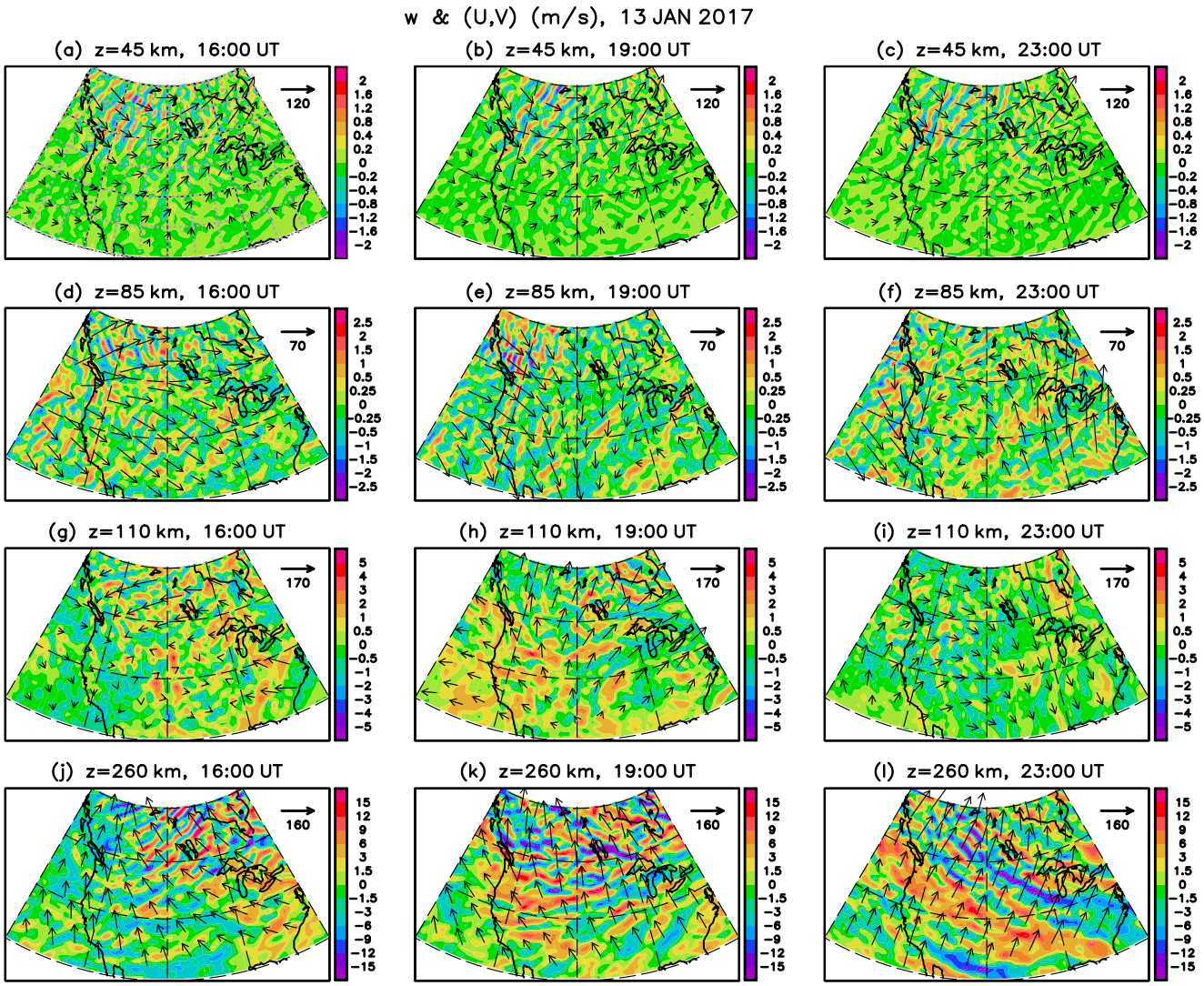


**Figure 7.** Same as Figure 6, but for 13 January 2017.

Figure 8 shows the simulated vertical wind (colors) and large-scale horizontal wind (black arrows) at different heights on 10, 11, and 13 January 2017 at 9 UT each day, that is, shortly after local midnight over North America. We picked this local time because no higher-order thermospheric GWs traveling over the pole from remote lower-thermospheric sources are expected around local midnight (see Figure 9 in Becker, Goncharenko, et al., 2022). On the other hand, poleward propagating higher-order GWs from MSVC caused by the MW event may occur at this local time. The first row ($z = 45$ km) confirms that there are persistent MWs in the stratosphere on 10 and 11 January, and that MWs are negligible on 13 January. Similar to our previous plots during the daytime, there are partial concentric ring structures of secondary gravity in the mesosphere at $z = 85$ km (second row) on 10 and 11 January, while these structures are insignificant on 13 January. In the lower thermosphere ($z = 110$ km, third row in Figure 8), the wind shears associated with the semi-diurnal tide induce the dissipation of the secondary GWs, which presumably also leads to feedbacks on the tidal winds. The major difference on 13 January to the earlier days is that GW structures are largely absent and the large-scale wind is much weaker. Both differences are consistent with the absence of MSVC on 13 January over the continental US and southern Canada as compared to the MV event during 11–12 January.

The fourth row in Figure 8 shows the GWs and large-scale flow at 260 km. Strong partial concentric ring structures are visible during the MW event. These GWs propagate away from the source region over the western US. The largest amplitudes are seen for northwestward to northward and northeastward propagation directions,

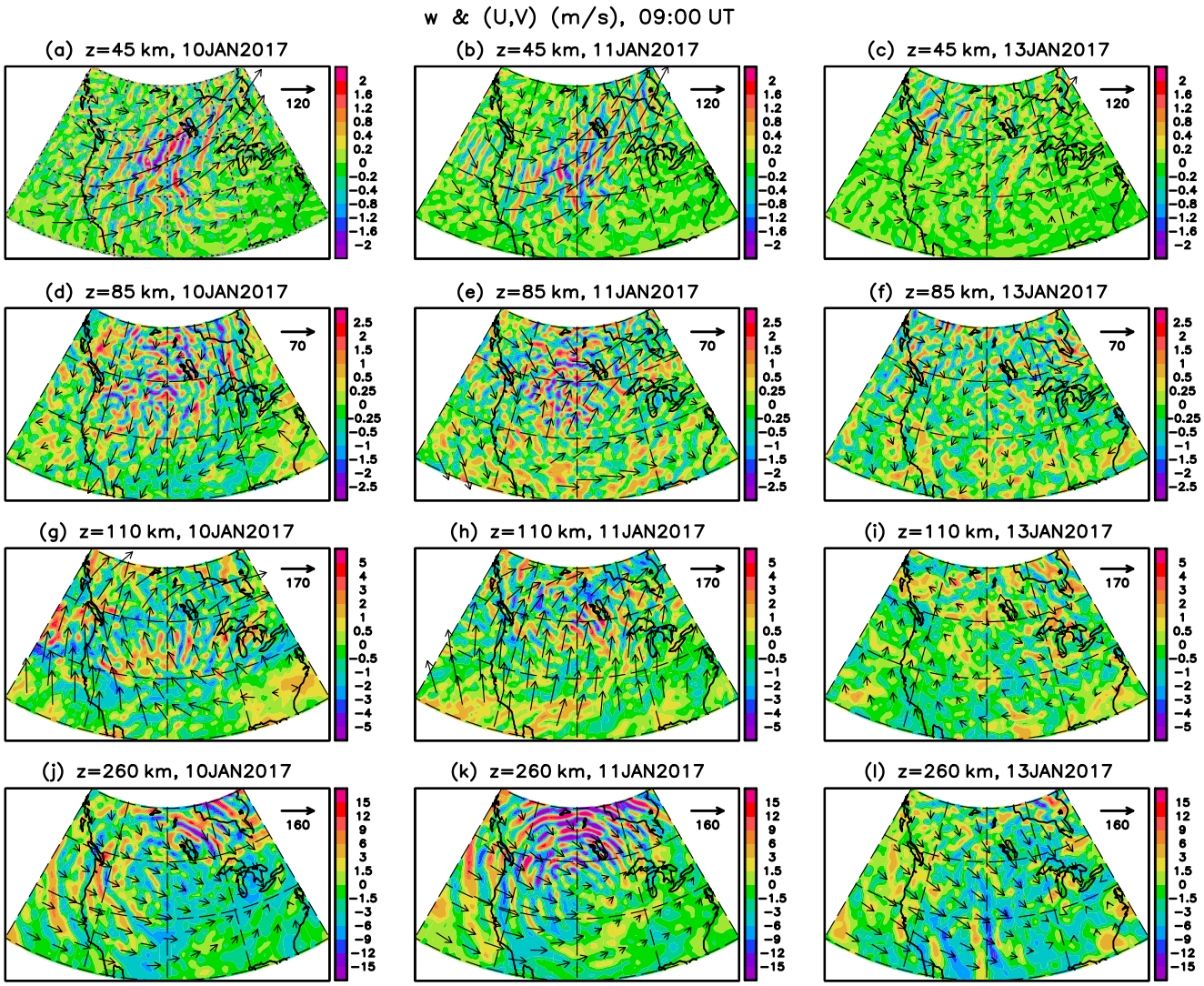


**Figure 8.** Horizontal slices over the continental US and southern Canada of the simulated vertical wind (colors) and the large-scale ($\lambda_h > 2000$ km) horizontal wind (arrows) at different heights (rows) and on different days in January 2017 at 9 UT. Left, middle, and right column: 10 January at 9 UT, 11 January at 9 UT, and 13 January at 9 UT. Upper to lower row: $z = 45$ km, $z = 85$ km, $z = 110$ km, and $z = 260$ km. The latitude is from 30°N to 60°N (latitude circles every 10°), and the longitude is from 135°W to 75°W with meridians every 15°. The arrow scale for the horizontal wind is given in the upper right corner of each panel in ms$^{-1}$. Note that the color and arrow scales differ from row to row.

particularly on 11 January (Figure 8k). Further inspection of model data showed that these higher-order GWs propagated over the polar region and appeared as southward propagating GWs over northern Europe and northern Russia around local noon (not shown). The fact that these partial concentric-type GWs are entirely absent after the MW event on 13 January (Figure 8l) is another strong indicator that these ring structures were caused by MSVC over the western US triggered by the MWs.

## 4. Multi-Step Vertical Coupling (MSVC) During the MW Event

The MSVC during the MW event can be illustrated by considering temporally and latitudinally averaged longitude-height plots of GW fluxes and their effects on the ambient flow. Figure 9a shows the GW potential energy flux per unit mass (colors). Using pressure as vertical coordinate, this flux is given by (e.g., Becker and Vadas, 2018)

$$F_p = -(g\,\bar{\rho})^{-1}\overline{\Phi'\omega'}. \quad (1)$$

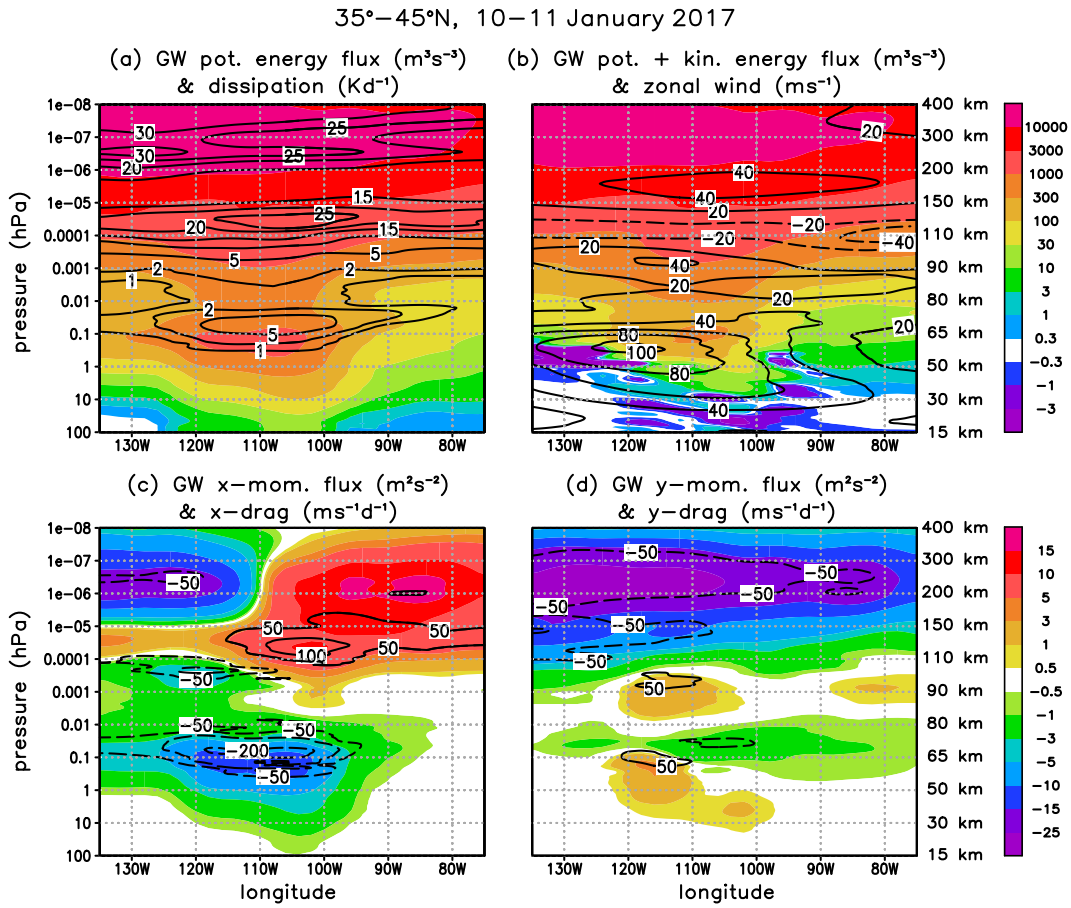


**Figure 9.** Gravity wave (GW) fluxes, zonal wind, and mean-flow effects averaged over the latitude band from 35° to 45°N and averaged from 0 UT on 10 January to 24 UT on 11 January 2017. (a) GW potential energy flux per unit mass (colors) and dissipation rate (black contours for $1, 2, 5, 10, 15, 20, 25, 30$ Kd$^{-1}$). (b) GW total energy flux per unit mass and zonal wind (black contours for $\pm 20$, $\pm 40$, $+60$, $+80$, $+100$ ms$^{-1}$). (c) GW zonal momentum flux per unit mass (colors) and drag (black contours for $-200$, $\pm 100$, $\pm 50$ ms$^{-1}$d$^{-1}$). (d) GW meridional momentum flux per unit mass (colors) and drag (black contours for $\pm 50$ ms$^{-1}$d$^{-1}$). See text for definitions.

Here, $g$ is the gravity acceleration, $\rho$ is density, $\Phi$ is the geopotential, and $\omega$ the pressure velocity. As usual, GW perturbations are indicated by primes and the average over the GW scales by a bar. Since the HIAMCM is a spectral model, we use the spectral transform method to define the large-scale flow by truncation at a total horizontal wavenumber of $n = 30$, which corresponds of a horizontal wavelength of $\lambda_h \approx 1350$ km. Accordingly, GW perturbations are defined by subtracting the large-scale flow from the fully resolved flow. As mentioned in Section 2, the HIAMCM is spectrally truncated at a total horizontal wavenumber of $n = 256$ ($\lambda_h \approx 156$ km). Using this method, we compute $\Phi'\omega'$ in gridspace, transform this GW second moment into spectral space, and then transform back into gridspace using a spectral truncation at $n = 80$ ($\lambda_h \approx 500$ km). Further temporal averaging over 3 hr then defines $\overline{\Phi'\omega'}$ in the case of the GW potential energy flux. The same method is applied to define other GW fluxes and flux divergences. In Figures 9 and 10, we further average model results from 35°N to 45°N and from 45°N to 60°N, respectively, as well as from 10 January at 0 UT to 11 January at 24 UT. This provides an average regional picture of the GW effects over the US and southern Canada during the MW event.

The GW potential energy flux per unit mass in Figure 9a (colors) increases with height from the troposphere to the stratopause, as is expected for vertically propagating primary GWs (including MWs). The maximum of this flux around 1 to 0.1 hPa ($z \sim 55$ km) and from about 120°W to 100°W indicates strong dissipation of the MWs. This is confirmed by the corresponding maximum of the mechanical dissipation rate per unit mass (turbulent frictional heating, for definition see Section 2 in Becker and Vadas (2020)) in this region, which is included in the figure by black contours. The dissipation rate per unit mass is maximum slightly above the flux maximum and roughly

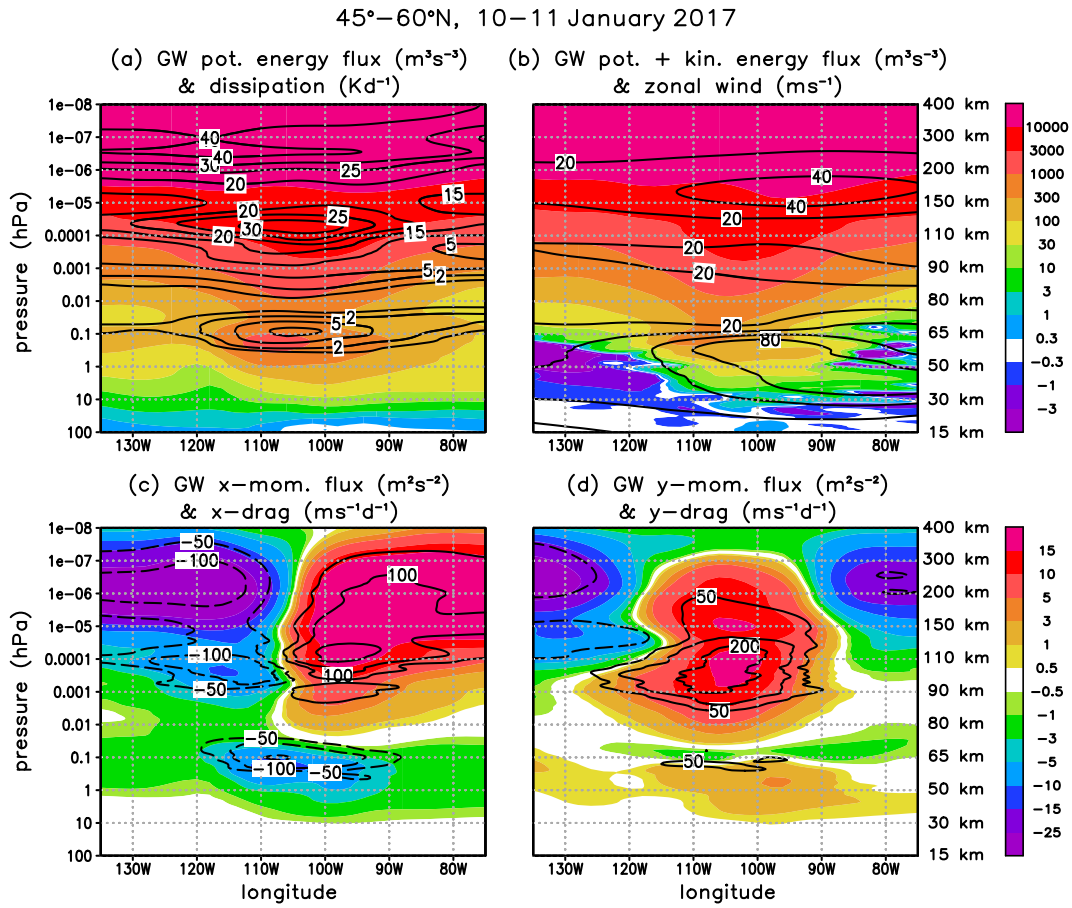


**Figure 10.** Same as Figure 9, but for the latitude band from 45°N to 60°N, and with contours in (a) for $1, 2, 5, 10, 15, 20, 35, 30, 40$ Kd$^{-1}$, in (b) for $+20$, $+40$, $+60$, $+80$ ms$^{-1}$, in (c) for $\pm 50$, $\pm 100$, $+200$ ms$^{-1}$d$^{-1}$, and in (d) for $\pm 50$, $+100$, $+200$ ms$^{-1}$d$^{-1}$.

coincides with the westward GW drag maximum in Figure 9c, as expected. Above about 0.01 hPa ($z \sim 80$ km), the potential energy flux increases again with altitude, indicating vertical propagation of secondary GWs that did not dissipate in the lower mesosphere. The pronounced second maximum of the dissipation rate between about $10^{-4}$ hPa and $10^{-5}$ hPa ($z \sim 110$ km to $z \sim 150$ km) indicates that these secondary GWs strongly dissipate in this region, giving rise to tertiary GWs. The further increase of the GW potenital energy flux with altitude in the thermosphere indicates the vertical propagation of the tertiary (or higher-order) GWs. In the HIAMCM, these GWs do not become dynamically unstable or break, but are damped continuously above about $10^{-6}$ hPa ($z \sim 200$ km) by molecular viscosity. This behavior is consistent with theory (Vadas, 2007) and former model estimates (Becker and Vadas, 2020).

The GW vertical flux of total (potential plus kinetic) energy per unit mass is defined in the pressure vertical coordinate system as (e.g., Becker and Vadas, 2018)

$$F_e = -(g\bar{\rho})^{-1}\left(\overline{\Phi'\omega'} + \bar{\mathbf{v}}\cdot\overline{\mathbf{v}'\omega'}\right). \quad (2)$$

Here, **v** denotes the horizontal wind vector. As discussed in Becker and Vadas (2018), MWs are characterized by a pronounced potential energy flux, while their total energy flux is close to zero. This is confirmed in Figure 9b for the MW event over the western US (note the nonlinear color scale used in the figure). From the mid mesosphere on (above about 0.03 hPa or $z \sim 70$ km), however, the total energy flux per unit mass strongly increases with height and is similar to the potential energy flux. This confirms that the GWs at these altitudes have significant

ground-based horizontal phase speeds. Hence, these GWs cannot be MWs, but must be secondary and higher-order GWs.

The second row in Figure 9 shows the eastward and northward components of the GW momentum flux per unit mass. In pressure coordinates, this momentum flux can be written as

$$\mathbf{F} = -(g\,\bar{\rho})^{-1}\,\overline{\mathbf{v}'\omega'}. \tag{3}$$

As expected for the MWs below the stratopause and given the strong eastward component of the tropospheric and stratospheric flow during the event (Figures 3c and 9b), there is strong westward momentum flux at $z \sim 30 - 70$ km (Figure 9c). Black contours in the lower row of the figure show the GW drag (momentum deposition) per unit mass, which is computed as $-\partial_p\,\overline{\mathbf{v}'\omega'}$ (e.g., Becker and Vadas, 2018). The westward maximum of the GW drag induced by MW disspation around 0.1 hPa ($z \sim 55$ km) and from 120°W to 100°W aligns with the corresponding local maximum of the dissipation rate in Figure 9a, as well as with strong westward vertical wind shear (contours in Figure 9b) which induces the dissipation of the MWs. Above the GW drag maximum in the lower mesosphere, the zonal momentum flux per unit mass is weak. It grows to significant values in the upper mesosphere due to the vertical propagation of the secondary GWs. Since these secondary GWs propagate away from the MW dissipation region into different horizontal directions, their momentum flux is eastward (westward) farther to the east (west), leading to eastward (westward) GW drag in the mesopause region and lower thermosphere. Similarly, the continuous dissipation of the tertiary GWs that propagate to altitudes above $10^{-6}$ hPa ($z \sim 200$ km) by molecular viscosity also leads to westward (eastward) momentum flux and drag farther to the west (east).

The meridional GW momentum flux and drag are shown in Figure 9d. There is some northward component of the MWs. The reason is that the flow in the lower troposphere had a significant southward component on 8 January and during the first half of 9 January as mentioned in Section 3. This southward wind component caused the MWs to have also a northward intrinsic propagation component. The secondary GWs show only a weak meridional momentum flux (and drag) in the lower mesosphere. The alternating signs from southward to northward with increasing height presumably results from several sources of the secondary waves and directional dissipation induced by the background wind such that different secondary GWs become predominant at different altitudes. Most importantly, the strong source region for tertiary GWs in the lower thermosphere that causes the partial concentric ring type structures of thermospheric GWs discussed in Section 3 implies that the meridional component of these GWs in the latitude band from 35°N to 45°N is southward, along with a southward GW drag when the tertiary GWs dissipate from molecular viscosity. This is confirmed by Figure 9d.

Figure 10 shows the averaged GW fluxes and effects as in Figure 9, but averaged from 45°N to 60°N. Regarding the energy fluxes and the dissipation rate (upper row), similar conclusions apply as for the latitude band from 35°N to 45°N. In particular, there is near-zero total energy flux from orographic GWs in the lower and mid stratosphere. The GW momentum flux and drag at 45°N to 60°N (lower row in Figure 10) shows westward and northward components in the stratopause region, which is consistent with the intrinsic MW propagation. Dissipation of the secondary GWs in the mesopause region shows again westward (eastward) momentum flux and drag farther to the west (east) from the MW region (Figure 10c). The same holds for the tertiary (or higher-order) GWs higher up in the thermosphere. Interestingly, the longitude regime from about 120°W to 90°W (for $z \sim 70 - 300$ km) in Figure 10d shows northward momentum flux and drag from the secondary and tertiary GWs. This is because the waves are generated as concentric structures that propagate away from the source region. Assuming that the source region for these secondary and tertiary GWs from the MW event is around 45°N (Figure 6, second and third rows), we expect northward momentum flux and drag in the upper mesosphere and farther above at 45°N to 60°N, and southward momentum flux and drag at 35°N to 45°N. Also note that west of about 120°W and east of about 90°W, the GWs in the upper thermosphere exhibit southward momentum flux and drag. This is because of the higher-order GWs from remote sources (e.g., over northern Siberia) that propagate over the pole and equatorward over North America during the daytime, as mentioned in Section 3.

Figure 11 shows the averaged momentum fluxes for the two latitude bands after the MW event (13–14 January). There is some westward GW drag in the mesosphere which is likely due to primary non-orographic GWs from either the troposphere or the polar vortex jet in the lower stratosphere, as well as weak eastward components in the mesopause region which reflects weak secondary GWs (Figures 11a and 11c). The thermosphere above $10^{-5}$ to

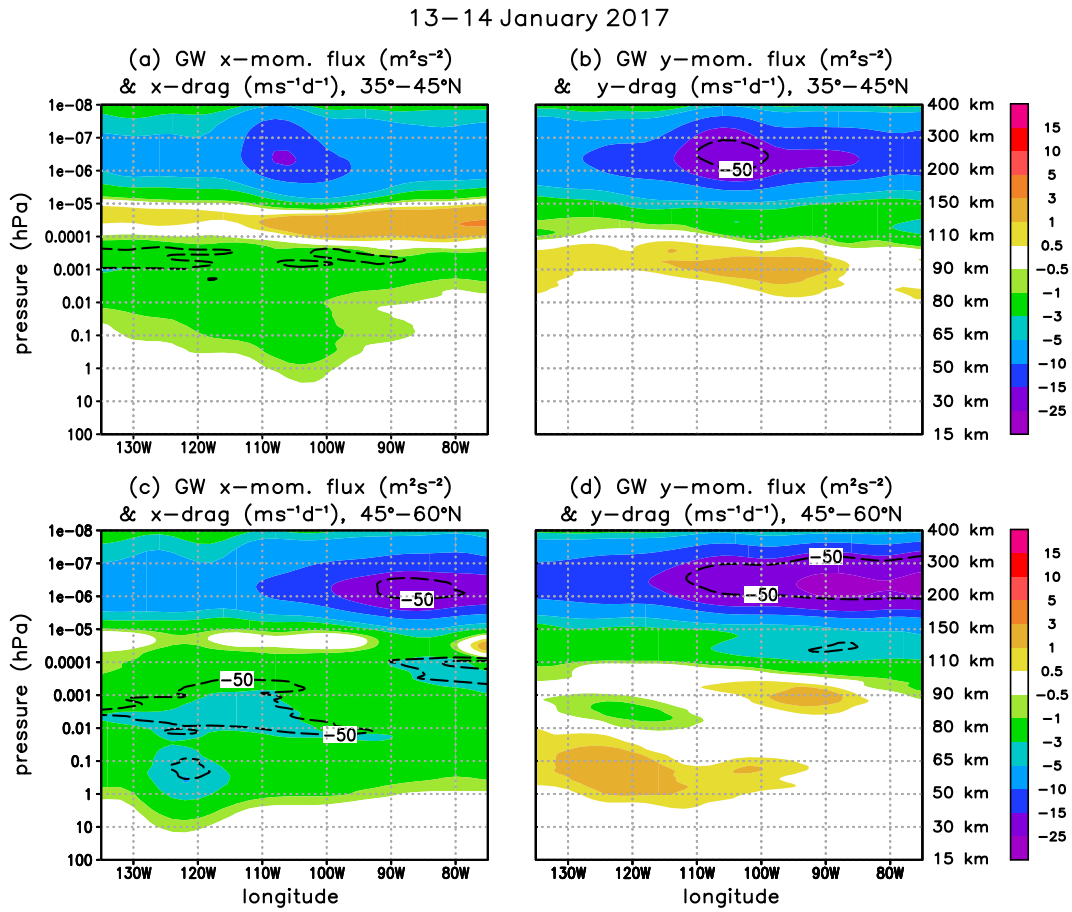


**Figure 11.** Gravity wave momentum flux per unit mass (colors) and drag components (black contour for $-50$ ms$^{-1}$d$^{-1}$) for 13–14 January 2017 over western North America and averaged from 35°N to 45°N (upper row) and from 45°N to 60°N (lower row). See text for definitions.

$10^{-6}$ hPa (about 150–200 km) shows significant southward momentum flux and drag in both latitude bands (Figures 11b and 11d). This reflects daytime tertiary (or higher-order) GWs from mainly remote sources. Overall, the averaged GW effects over North America are much weaker than during the MW event. This pertains also to the energy fluxes and the dissipation rate (not shown).

## 5. Comparison of Simulated GWs With Ionospheric Data

In Sections 3 and 4 we showed that the simulated GWs in the thermosphere over North America during January 2017 are consistent with MSVC caused by a MW event over the western US from January 8 to 11. In the following we show that these model results are consistent with the observed TIDs.

The first row in Figure 12 shows the vertical wind (colors) and the large-scale horizontal wind (black arrows) on 10 January (during the MW event) from the HIAMCM at $z = 260$ km for three consecutive times from local morning to local afternoon over the continental US. The rotation of the tidal flow from northwestward (18 UT) to northward (20:30 UT) and to northeastward (23 UT) is clearly seen. Partial concentric ring structures of GWs are evident in the vertical wind at each time. As discussed in Section 3, different apparent propagation directions have the largest amplitude depending on the tidal flow (local time). More specifically, there is predominantly eastward to southeastward propagation at 18 UT over the northeastern US, southward propagation at 20:30 UT over the central US, and southwestward propagation at 23 UT over the northwestern US. Some apparent centers of these structures in Figures 12a–12c are over the northwestern US and over southwest Canada. Hence, there is a northward displacement of the tertiary GW sources from the MW source region. Such a displacement can occur

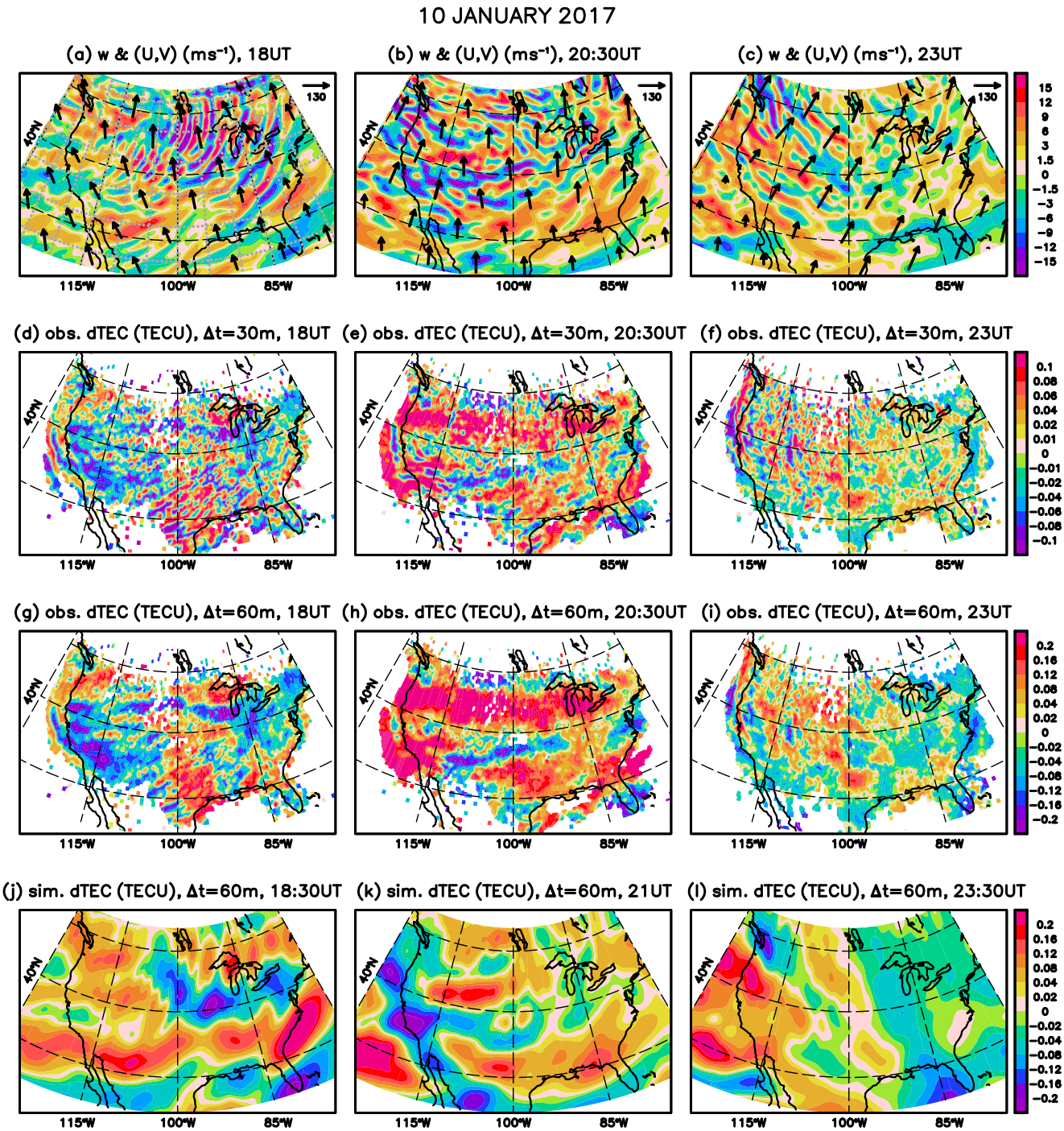


**Figure 12.** Thermospheric gravity waves and ionospheric disturbances around local noon during the mountain wave event. First row: Vertical wind (colors) and large-scale horizontal wind ($\lambda_h > 2000$ km, black arrows) from the HIAMCM at $z = 260$ km on 10 January 2017 at 18:00, 20:30, and 23:00 UT (from left to right). Second row: Observed perturbations of the TEC (dTEC) according to the method described in Section 2 at the same universal times as in the first row. A running mean over 30 min has been subtracted from the TEC. Third row: Same as second row, but for a running mean of 60 min. Fourth row: Simulated dTEC from the SAMI3 driven by the neutral winds from the HIAMCM for universal times shifted forward by 30 min relative to rows 1–3. A running mean over 60 min has been subtracted from the simulated TEC.

when the secondary GWs propagate farther northward before they dissipate in the lower thermosphere. Around local noon (Figure 12b), the GWs with long $\lambda_h$ exhibit curved phases with radii that are too large for the centers to be located over the northwestern US or southwest Canada. Rather, these GWs emerge from remote sources over

northern Europe and northern Siberia, propagate over the polar region, and appear as southward GWs over North America, as discussed in Section 3.

The second row in Figure 12 shows the observed dTEC based on the methodology described in Section 2 with a 30 min running-mean filter. The resulting dTEC includes roughly all wave periods smaller than about 1 hr. This dTEC was furthermore horizontally smoothed by substituting each grid-point value by the mean of this value and the values at the 4 neighboring grid points (missing data points were not included). The apparent propagation directions of the wave structures in the observed dTEC are roughly as for the GWs in the model. This refers to southeastward to southward propagating waves over the southern US at 18 UT and 20:30 UT, respectively, as well as westward waves over the west coast of the US at 23 UT. Also note that the GPS data show smaller-scale structures than the simulated vertical wind. This is in part due to noise in the dTEC caused by observation errors and the applied postprocessing methods. It is also likely that the observed dTEC includes small-scale GW structures that are not resolved by the HIAMCM. The third row in Figure 12 shows the observed dTEC as in the second row, but with a running-mean filter of 1 hr, thereby emphasizing larger-scale waves (e.g., the LSTIDs from auroral forcing). The observed large scales of the TIDs at 20:30 UT (Figures 12e and 12h) are not visible in the vertical wind from the model. It is tempting to interpret these LSTIDs as a result from auroral activity as mentioned in Section 2.

The fourth row in Figure 12 shows the dTEC from the SAMI3 simulation driven by the neutral winds from the HIAMCM as described in Section 2. This dTEC is derived from the simulated TEC by subtracting a running mean of 1 hr (reflecting wave periods shorter than about 2 hr). The horizontal scales resolved by the SAMI3 are larger than those resolved by the HIAMCM, and are much larger than the scales visible in the observed dTEC with a 30 min running-mean filter. We therefore compare the dTEC from the SAMI3 with the observed dTEC in the third row of Figure 12. To improve this comparison, we plot the SAMI3 results 30 min later than in rows 1–3, namely at 18:30, 21, and 23:30 UT in Figures 12j, 12k, and 12l, respectively. The apparent propagation directions and amplitudes of the simulated TIDs agree reasonably well with the observed dTEC. This is remarkable since these LSTIDs are produced by the SAMI3 as a result of MSVC as simulated by the HIAMCM; auroral forcing of GWs is neither included in the HIAMCM nor in the SAMI3. Particularly the southward propagating large-scale waves over the midwest and the east coast of the US at 18 (18:30) UT and 20:30 (21) UT show reasonable agreement. This suggests that the auroral forcing during the second half of 10 January (Figure 1d) plays only a moderate role for the observed TIDs depicted in Figures 12g and 12h.

Figure 13 shows the comparison of simulated GWs with observed and simulated dTEC for 11 January. The first row suggests that on this day, the apparent centers of the partial concentric ring structures at 18 UT and 21:30 UT are somewhat to the west of the Rocky Mountains, while the structure at 23 UT (Figure 13c) is centered somewhat to the east. Interestingly, the simulated tertiary (or higher-order) GWs related to these ring structures do not clearly show maximum amplitudes for propagation directions against the large-scale (tidal) wind. The reason could be that the body forces giving rise to these structures are at higher altitudes than on 10 January such that the dissipation of GWs propagating with the tidal winds is less efficient. The observed dTEC with a 30 min running-mean filter (second row) reflects the simulated concentric-ring-type GWs as MSTIDs, particularly at 20:30 and 23 UT (compare Figures 13e and 13f to Figures 13b and 13c, respectively). Moreover, larger-scale GWs are seen farther away from the centers of these ring structures in the simulated vertical wind and in the observed dTEC at 20:30 UT and 23 UT, for example, over the southeastern US. These larger-scale GWs typically have larger phase speeds than the medium-scale GWs from the same sources in the lower thermosphere and are therefore seen at greater distances (Vadas and Azeem, 2021; Vadas et al., 2024).

Again, medium-to-large-scale TIDs are emphasized when a 60 min running-mean filter is applied to the observed TEC (third row in Figure 13). While these medium-to-large-scale wave structures are not well captured by the SAMI3 at 18 UT (Figure 13g), better agreement is seen at 20:30 and 23 UT. For example, southward propagating large-scale waves are evident over the western US at 20:30 and 23 UT in both the observed and simulated dTEC. These TIDs appear to advance to the east from 20:30 to 23 UT. Furthermore, there are southeastward propagating wave phases over the eastern US where the SAMI3 captures some of the individual dTEC minima and maxima. Overall, the comparison of the simulated and observed TIDs is better than on 10 January. This is expected because auroral forcing was small on 11 January (see Section 2 and Figure 1).

It is important to compare the simulated GWs with the observed TIDs after the MW event. Unfortunately, we have SAMI3 results only up until 11 January. Therefore, we compare in Figure 14 the simulated GWs with the

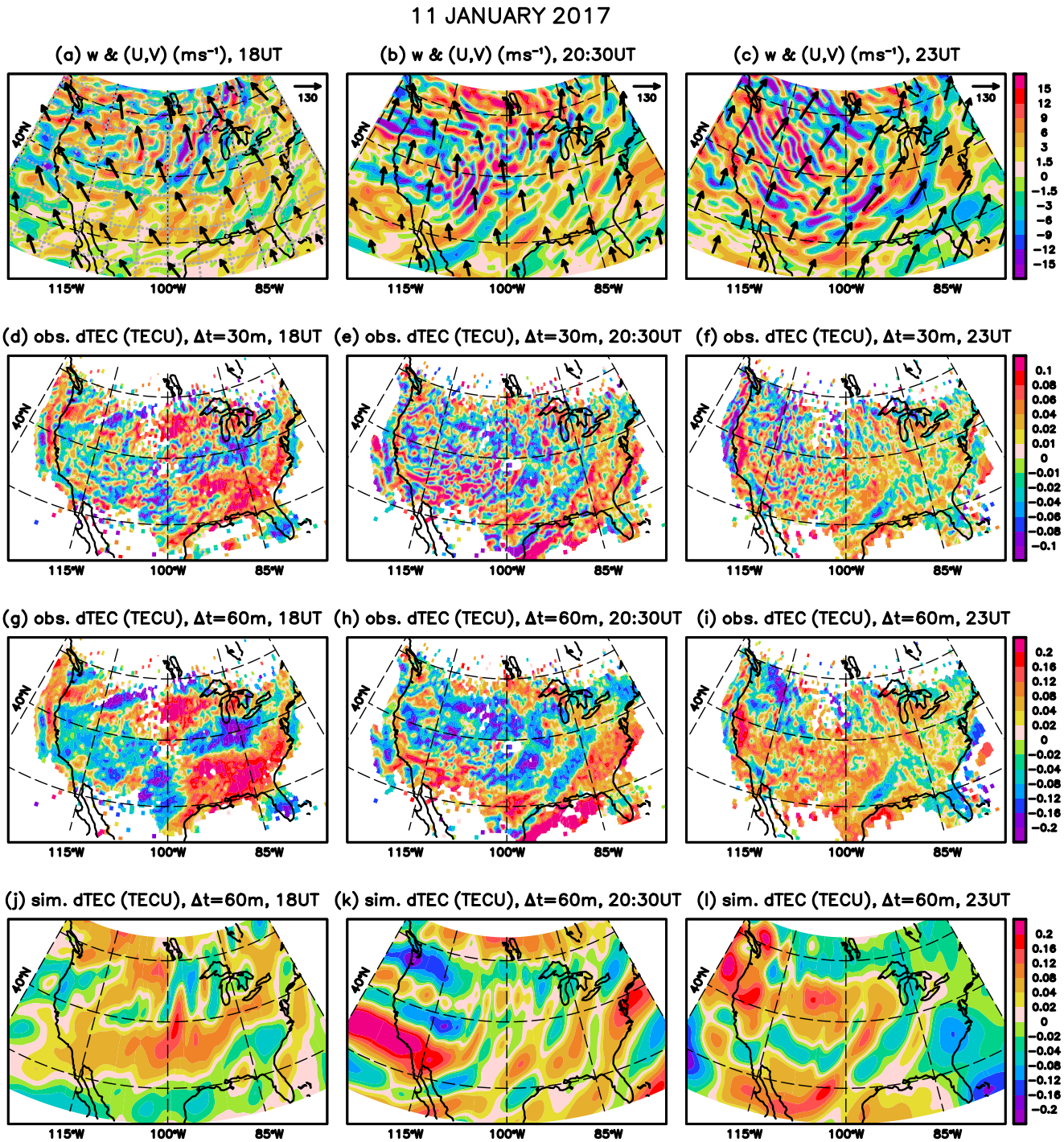


**Figure 13.** Same as Figure 12, but for 11 January 2017 and with the SAMI3 dTEC shown at 18, 20:30, and 23 UT.

observed dTEC for 13 January. The simulated vertical wind mainly shows medium-to-large-scale GWs with apparent southeastward to southwestward propagation directions (first row) with amplitudes weaker than in Figure 13. The amplitudes of the medium-scale waves in the dTEC (second row) are at most about half as strong as on 10 and 11 January. In particular, there is no indication of partial concentric ring structures over the western US and southwest Canada. Instead, there are some medium-to-large-scale waves with apparent southwestward to southeastward propagation directions, where the latter are more prominent when a 60 min running-mean filter is applied (third row in Figure 14). Again, these waves are indicative of MSVC in other regions of the northern

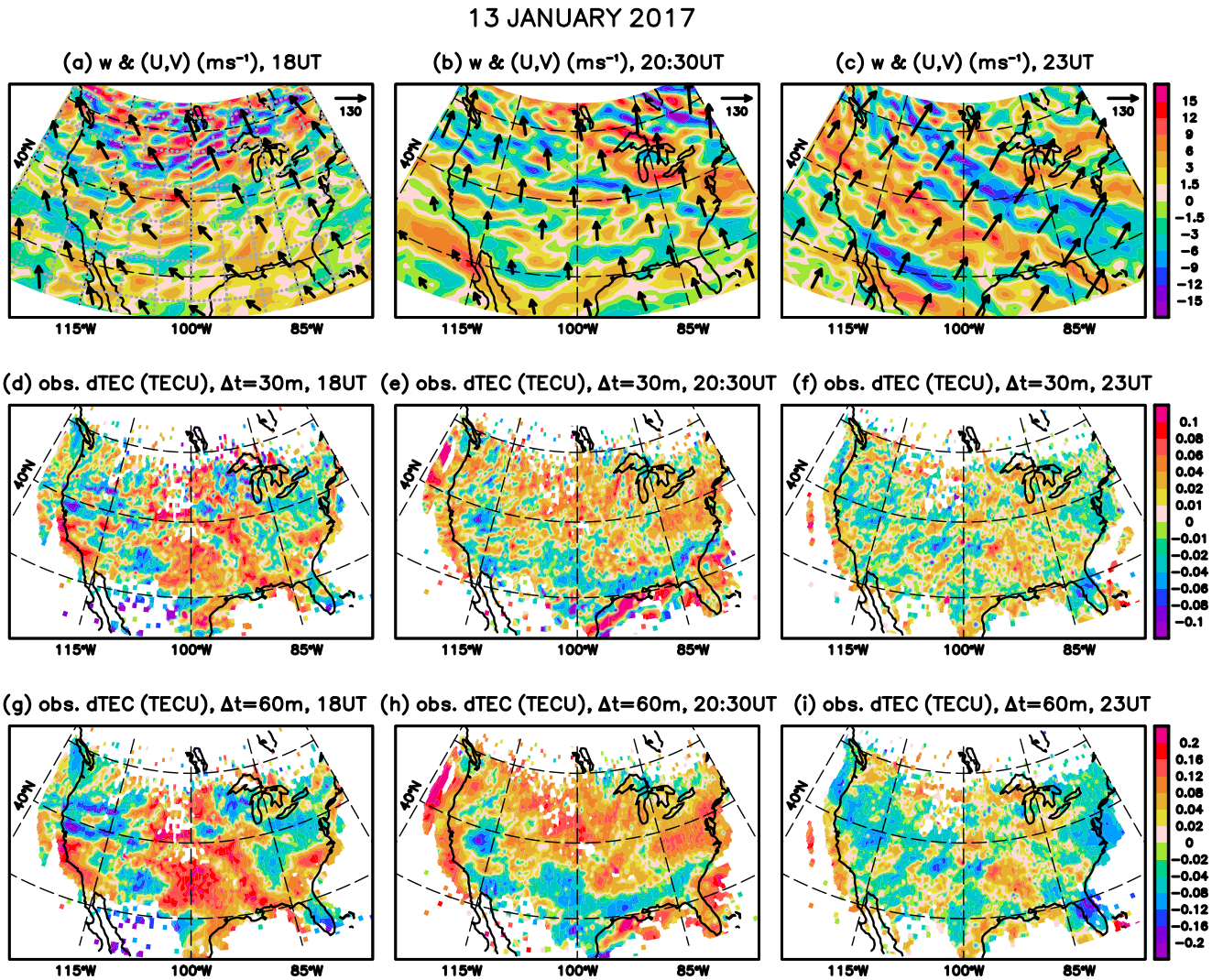


**Figure 14.** Same as rows 1–3 in Figure 12, but for 13 January 2017.

hemisphere. The phases of these wave structures align with the simulated GW phases only in certain regions during certain times, for example, over California and northeastern Mexico at 18 UT, from southern Texas to Florida at 20:30 UT, and over the northeastern US at 23 UT.

## 6. Summary

We analyzed an event of strong orographic gravity-wave (GW) activity over the western US in January 2017 using the HIAMCM, the ionospheric model SAMI3, and GPS TEC data. We found that medium-scale mountains waves (MWs) were generated by strong eastward tropospheric flow over the Sierra Nevada and the Rocky Mountains from 9 to 11 January, and that the stratospheric polar vortex jet extended from the western US to eastern Canada during that time such that the MWs propagated into the middle atmosphere. We showed that the dissipation of the MWs in the stratopause region and lower mesosphere resulted in the generation of secondary GWs that propagated further upward. In turn, the dissipation of the secondary waves in the upper MLT gave rise to concentric-ring-type tertiary GWs centered over the western US. A higher altitudes in thermosphere, certain propagation directions of the tertiary GWs were highlighted during certain local times as a result of the dissipation induced by the diurnal tidal winds. More specifically, at $z = 260$ km we find southeastward propagating GWs during local morning over the eastern US, equatorward propagation around local noon over the southern US, and southwestward and westward GWs propagation around local afternoon over the western US. In addition, the

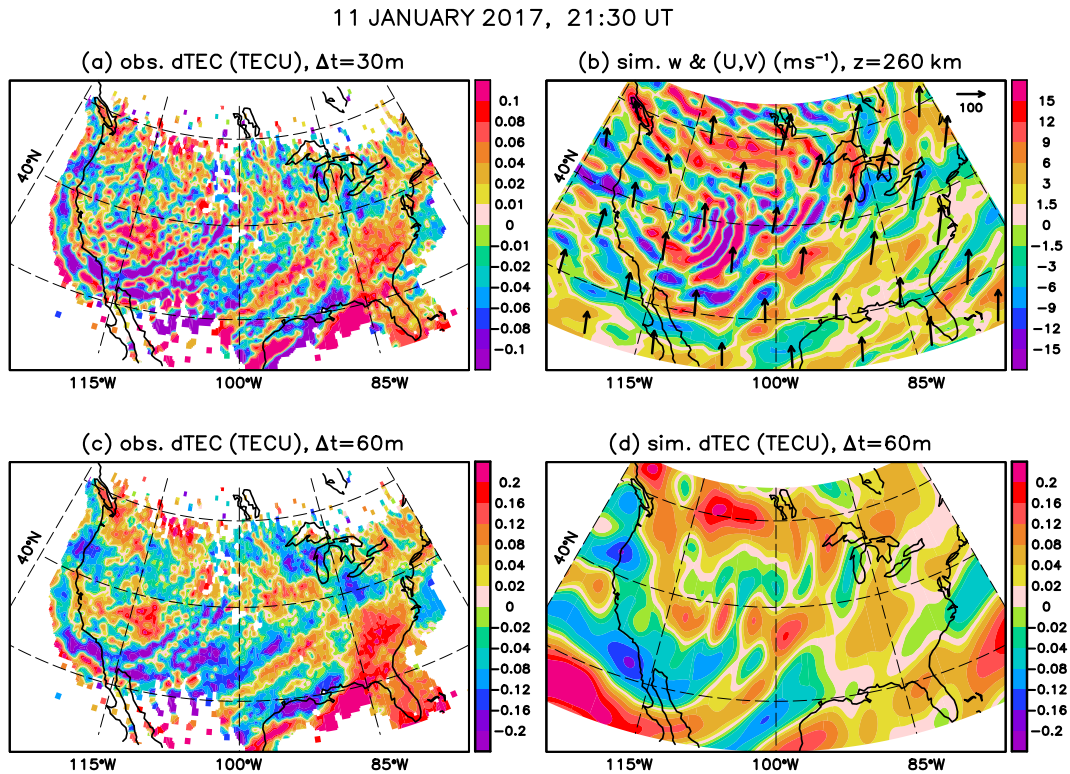


**Figure 15.** Thermospheric gravity waves and TIDs on 11 January 2017 at 21:30 UT. (a) Observed dTEC obtained by subtracting a running mean over 30 min from the TEC. (b) Vertical wind (colors) and large-scale horizontal wind ($\lambda_h > 2000$ km, black arrows) from the HIgh Altitude mechanistic General Circulation Model (HIAMCM) at $z = 260$ km. (c) Same as (a), but for a running mean of 60 min. (d) Simulated dTEC from the SAMI3 driven by the neutral winds from the HIAMCM (a running mean over 60 min has been subtracted from the simulated TEC).

HIAMCM shows poleward propagation of GWs over Canada after local midnight. This pattern roughly repeated itself for several days during the MW event. In addition, there were equatorward propagating GWs around local noon from remote sources during and after the MW event.

We performed detailed analysis of the regional GW fluxes of momentum and energy, and we computed the resulting regional GW effects on the ambient larger-scale flow, that is, the regional momentum deposition and mechanical dissipation rate. This analysis confirmed that the MSVC mechanism as described above was indeed triggered by (quasi-stationary) MWs from flow over the mountain ridges in the western US. In particular, the momentum fluxes showed that the secondary and tertiary GWs caused by the MWs propagated away from the source regions into various directions, and that these propagation directions were consistent with the partial concentric ring structures.

The ionospheric disturbances as simulated by the ionospheric model SAMI3 driven by the neutral winds from the HIAMCM were found to be consistent with the LSTIDs over the continental US deduced from TEC data. In addition, some geomagnetic activity on 10 January that was not included in our model simulations was visible in the observations. On 11 January, auroral forcing of GWs did not play a role based on the time series of various geomagnetic indices. On this day, the SAMI3 simulated the LSTIDs with roughly realistic amplitudes (in total electron content disturbances) and even with roughly the correct wave phases (Figure 13). These results are summarized in Figure 15, showing model and observational results at 21:30 UT on 11 January 2017. At this time, the concentric-ring structures in the observed dTEC with a 30 min running-mean filter and the GWs simulated by the HIAMCM look very similar (upper row), and the SAMI3-HIAMCM result for the dTEC is largely consistent with the observed dTEC with a 60 min running-mean filter as well (lower row). We showed in Figures 11 and 14 that after the MW event, the GW effects and associated concentric-ring-type GWs in the thermosphere vanished in the HIAMCM and in the observed dTEC.

This paper investigates an episode in January 2017 where strong MWs generated over the western US very likely led to concentric-ring type TIDs in the F region. Another case study of this kind was recently published by Inchin et al. (2024) for a MW event over the western US in December 2022. Unlike their suggestion that the MWs dissipated in the mesopause region from critical levels and that secondary GWs gave rise to the observed concentric-ring structures in the F region, our GW-resolving whole atmosphere modeling shows that strong, medium-scale MWs dissipated in the stratopause region and lower mesosphere, and that the concentric-ring structures in the F region most likely resulted from tertiary or even higher-order GWs. It is currently not known how often such wintertime MW events with significant effects on the F region occur. The usual northern hemispheric winter circulation during periods with a moderate-to-strong polar vortex is characterized by a GW hotspot in the upper stratosphere over Europe rather than over the western US (e.g., Becker, Vadas et al., 2022; Hoffmann et al., 2014; Harvey et al., 2023; Vadas et al., 2023, 2024). Therefore, wintertime events of MSVC from MWs are expected to be less frequent over the western US than over Europe. Nevertheless, our results suggest that it should be possible to anticipate MSVC effects in the thermosphere/ionosphere from wintertime MW events over the Rocky Mountains and other mountain ranges in Europe and Asia. To this end one would need to couple forecasts for the troposphere and stratosphere to a GW-resolving whole-atmosphere model that consistently and accurately includes the MSVC mechanism and is coupled to an ionospheric model.

## Data Availability Statement

Model simulations were performed at the NASA High-End Computing Capability. Model documentations can be found in Section 2 and the papers cited therein. The MERRA-2 reanalyzes used in this study are publicly available at https://goldsmr5.gesdisc.eosdis.nasa.gov/data/MERRA2/M2I3NPASM.5.12.4. Solar Wind Data was acquired from OMNIWeb https://omniweb.gsfc.nasa.gov. The Kp Index was acquired from GFZ Potsdam: https://kp.gfz-potsdam.de/en. SMR, SML, and SMU geomagnetic indices were acquired from SuperMag: https://supermag.jhuapl.edu. GNSS RINEX files were acquired from EarthScope https://www.earthscope.org/data, NOAA CORS https://geodesy.noaa.gov/corsdata, and NASA CDDIS https://cddis.nasa.gov/Data_and_Derived_Products/GNSS/daily_30second_data.html. All model data shown in this study are available via NWRA's website under https://www.cora.nwra.com/~erich.becker/Becker-Mrak-etal-JGRSP-2025-files.

**Acknowledgments**
EB and SLV were supported by NSF Grant 2329957, NASA Grant 80NSSC22K0174, and ONR Grant N00014-24-1-2367. EB was furthermore supported by NASA Grant 80NSSC21M0180. SM was supported by NSF Grants 2329957 and AGS-2407263, as well by ONR Grant N00014-24-1-2329. JDH was supported by NASA Grants 80NSSC22K0174 and 80NSSC21K1305. The comments of two anonymous reviewers are gratefully acknowledged.

## References

Alexander, M. J., Geller, M., McLandress, C., Polavarapu, S., Preusse, P., Sassi, F., et al. (2010). Recent developments in gravity-wave effects in climate models and the global distribution of gravity-wave momentum flux from observations and models. *Quarterly Journal of the Royal Meteorological Society*, *136*(650), 1103–1124. https://doi.org/10.1002/qj.637

Alexander, S. P., Sato, K., Watanabe, S., Kawatani, Y., & Murphy, D. J. (2016). Southern hemisphere extratropical gravity wave sources and intermittency revealed by a middle-atmosphere general circulation model. *Journal of the Atmospheric Sciences*, *73*(3), 1335–1349. https://doi.org/10.1175/JAS-D-15-0149.1

Azeem, I., Yue, J., Hoffmann, L., Miller, S. D. W. C. S., III, & Crowley, G. (2013). Multisensor profiling of a concentric gravity wave event propagating from the troposphere to the ionosphere. *Geophysical Research Letters*, *42*(19), 7874–7880. https://doi.org/10.1002/2015GL065903

Becker, E., Garcia, R., Pedatella, N., Vadas, S., & Yudin, V. (2023). Explicit simulation of gravity waves in whole atmosphere models. *Bulletin of the AAS*, *55*(3). https://doi.org/10.3847/25c2cfeb.e4e59438

Becker, E., Goncharenko, L., Harvey, V. L., & Vadas, S. L. (2022). Multi-step vertical coupling during the January 2017 sudden stratospheric warming. *Journal of Geophysical Research: Space Physics*, *127*(12), e2022JA030866. https://doi.org/10.1029/2022JA030866

Becker, E., & Oberheide, J. (2023). Unexpected DE3 tide in the southern summer mesosphere. *Geophysical Research Letters*, *50*(20), e2023GL104368. https://doi.org/10.1029/2023GL104368

Becker, E., & Vadas, S. L. (2018). Secondary gravity waves in the winter mesosphere: Results from a high-resolution global circulation model. *Journal of Geophysical Research: Atmospheres*, *123*(5), 2605–2627. https://doi.org/10.1002/2017JD027460

Becker, E., & Vadas, S. L. (2020). Explicit global simulation of gravity waves in the thermosphere. *Journal of Geophysical Research: Space Physics*, *125*(10), e2020JA028034. https://doi.org/10.1029/2020JA028034

Becker, E., Vadas, S. L., Bossert, K., Harvey, V. L., Zülicke, C., & Hoffmann, L. (2022). A high-resolution whole-atmosphere model with resolved gravity waves and specified large-scale dynamics in the troposphere and stratosphere. *Journal of Geophysical Research: Atmospheres*, *127*(2), e2021JD035018. https://doi.org/10.1029/2021JD035018

Becker, E., Vadas, S. L., & Chu, X. (2024). Multi-step vertical coupling via gravity waves from the lower to the upper atmosphere. In R. Lieberman (Ed.), *Reference module in Earth systems and environmental sciences*. Elsevier. https://doi.org/10.1016/B978-0-323-96026-7.00159-4

Bosilovich, M. G., Akella, S., Coy, L., Cullather, R., Draper, C., Gelaro, R., et al. (2015). MERRA-2: Initial evaluation of the climate. NASA Tech. Rep. In *Series on global modeling and data assimilation*. Goddard Space Flight Center. NASA/TM-2015-104606/Vol. 43.

Frissell, N. A., Baker, J. B. H., Ruohoniemi, J. M., Greenwald1, R. A., Gerrard, A. J., Miller, E. S., & West, M. L. (2016). Sources and characteristics of medium-scale traveling ionospheric disturbances observed by high-frequency radars in the north American sector. *Journal of Geophysical Research: Space Physics*, *121*(4), 3722–3739. https://doi.org/10.1002/2015JA022168

Fritts, D. C., Smith, R. B., Taylor, M. J., Doyle, J. D., Eckermann, S. D., Dörnbrack, A., et al. (2016). The deep propagating gravity wave experiment (DEEPWAVE): An airborne and ground-based exploration of gravity wave propagation and effects from their sources throughout the lower and middle atmosphere. *Bulletin America Meteorology Social*, *97*(3), 425–453. https://doi.org/10.1175/BAMS-D-14-00269.1

Gelaro, R., McCarty, W., Suárez, M. J., Todling, R., Molod, A., Takacs, L., et al. (2017). The Modern-Era retrospective analysis for research and applications, version 2 (MERRA-2). *Journal of Climate*, *30*(13), 5419–5453. https://doi.org/10.1175/JCLI-D-16-0758.1

Hain, K. (1987). The partial donor cell method. *Journal of Computational Physics*, *73*(1), 131–147. https://doi.org/10.1016/0021-9991(87)90110-0

Harvey, V. L., Pedatella, N., Becker, E., & Randall, C. E. (2022). Evaluation of polar winter mesopause wind in WACCMX+DART. *Journal of Geophysical Research: Atmospheres*, *127*(15), e2022JD037063. https://doi.org/10.1029/2022JD037063

Harvey, V. L., Randall, C. E., Goncharenko, L. P., Becker, E., Forbes, J. M., Carstens, J., et al. (2023). CIPS observations of gravity wave activity at the edge of the polar vortices and coupling to the ionosphere. *Journal of Geophysical Research: Atmospheres*, *128*(12), e2023JD038827. https://doi.org/10.1029/2023JD038827

Heale, C. J., Inchin, P. A., & Snively, J. B. (2022). Primary versus secondary gravity wave responses at F-region heights generated by a convective source. *Journal of Geophysical Research: Atmospheres*, *127*(1), e2021JA029947. https://doi.org/10.1029/2021ja029947

Hindley, N. P., Mitchell, N. J., Cobbett, N., Smith, A. K., Fritts, D. C., Janches, D., et al. (2022). Radar observations of winds, waves and tides in the mesosphere and lower thermosphere over South Georgia Island (54°s, 36°w) and comparison to WACCM simulations. *Atmospheric Chemistry and Physics*, 9435–9459. https://doi.org/10.5194/acp-2021-981

Hindley, N. P., Wright, C. J., Gadian, A. M., Hoffmann, L., Hughes, J. K., Jackson, D. R., et al. (2020). Stratospheric gravity-waves over the mountainous island of southgeorgia: Testing a high-resolution dynamical model with 3-d satellite observations and radiosondes. *Atmospheric Chemistry and Physics*, 7695–7722. https://doi.org/10.5194/acp-2020-465

Hoffmann, L., Alexander, M. J., Clerbaux, C., Grimsdell, A. W., Meyer, C. I., Robler, T., & Tournier, B. (2014). Intercomparison of stratospheric gravity wave observations with AIRS and IASI. *Atmospheric Measurement Techniques*, *7*(12), 4517–4537. https://doi.org/10.5194/amt-7-4517-2014

Huba, J. D. (2003). Hall magnetohydrodynamics - A tutorial, in space plasma simulation. In M. Scholer, C. T. Dum, & J. Büchner (Eds.), *Lecture notes in physics* (Vol. 615, 166–192). Springer. https://doi.org/10.1007/3-540-36530-3_9

Huba, J. D., Becker, E., & Vadas, S. L. (2023). Simulation study of the 15 January 2022 Tonga event: Development of super equatorial plasma bubbles. *Geophysical Research Letters*, *50*(1), e2022GL101185. https://doi.org/10.1029/2022GL101185

Huba, J. D., Joyce, G., & Fedder, J. A. (2000). Sami2 (Sami2 is another model of the ionosphere): A new low-latitude ionosphere model. *Journal of Geophysical Research*, *105*(A10), 23035–23053. https://doi.org/10.1029/2000ja000035

Huba, J. D., Joyce, G., & Krall, J. (2008). Three-dimensional equatorial spread F modeling. *Geophysical Research Letters*, *45*, L10102. https://doi.org/10.1029/2008GL033509

Inchin, P. A., Bhatt, A., Bramberger, M., Chakraborty, S., Debchoudhury, S., & Heale, C. (2024). Atmospheric and ionospheric responses to orographic gravity waves prior to the December 2022 cold air outbreak. *Journal of Geophysical Research: Space Physics*, *129*(6), e2024JA032485. https://doi.org/10.1029/2024JA032485

Kogure, M., Chou, M., Yue, J., Otsuka, Y., Liu, H., Sassi, F., et al. (2024). Medium-scale traveling ionospheric disturbances created by primary gravity waves generated by a winter storm. *J. Space Weather Space Clim.*, *14*, 38. https://doi.org/10.1051/swsc/2024036

Kogure, M., Yue, J., Chou, M., Liu, H., Otsuka, Y., Randall, C. E., et al. (2025). Coincident/simultaneous observations of stratospheric concentric gravity waves and concentric traveling ionospheric disturbances over the continental U.S. in 2022. *Journal of Geophysical Research: Space Physics*, *130*(3), e2024JA033429. https://doi.org/10.1029/2024JA033429

Kruse, C. G., Alexander, M. J., Hoffmann, L., van Niekerk, A., Polichtchouk, I., Bacmeister, J. T., et al. (2022). Observed and modeled mountain waves from the surface to the mesosphere near the Drake Passage. *Journal of the Atmospheric Sciences*, *79*(4), 909–932. https://doi.org/10.1175/JAS-D-21-0252.1

Lund, T. S., Fritts, D. C., Wan, K., Laughman, B., & Liu, H.-L. (2020). Numerical simulation of mountain waves over the Southern Andes. Part I: Mountain wave and secondary wave character, evolutions, and breaking. *Journal of the Atmospheric Sciences*, *77*(12), 4337–4356. https://doi.org/10.1175/JAS-D-19-0356.1

Lyons, L. R., Nishimura, Y., Zhang, S.-R., Coster, A. J., Bhatt, A., Kendall, E., & Deng, Y. (2019). Identification of auroral zone activity driving large-scale traveling ionospheric disturbances. *Journal of Geophysical Research: Space Physics*, *124*(1), 700–714. https://doi.org/10.1029/2018JA025980

McLandress, C., Scinocca, J. F., Shepherd, T. G., Reader, M. C., & Manney, G. L. (2013). Dynamical control of the mesosphere by orographic and nonorographic gravity wave drag during the extended northern winters of 2006 and 2009. *Journal of the Atmospheric Sciences*, *70*(7), 2152–2169. https://doi.org/10.1175/JAS-D-12-0297.1

Mrak, S., Semeter, J., Nishimura, Y., & Coster, A. J. (2021). Extreme low-latitude total electron content enhancement and global positioning system scintillation at dawn. *Space Weather*, *9*, e2021SW002740. https://doi.org/10.1029/2021SW002740

Nayak, C., & Yiğit, E. (2019). Variation of small-scale gravity wave activity in the ionosphere during the major sudden stratospheric warming event of 2009. *Journal of Geophysical Research: Space Physics*, *124*(1), 470–488. https://doi.org/10.1029/2018JA026048

Nicolls, M. J., Vadas, S. L., Aponte, N., & Sulzer, M. P. (2014). Horizontal wave parameters of daytime thermospheric gravity waves and E region neutral winds over Puerto Rico. *Journal of Geophysical Research*, *119*(1), 575–600. https://doi.org/10.1002/2013JA018988

Nishioka, M., Tsugawa, T., Kubota, M., & Ishii, M. (2013). Concentric waves and short-period oscillations observed in the ionosphere after the 2013 Moore EF5 tornado. *Geophysical Research Letters*, *40*(21), 5581–5586. https://doi.org/10.1002/2013GL057963

Noble, P. E., Hindley, N. P., Wright, C. J., Cullens, C., England, S., Pedatella, N., et al. (2024). Interannual variability of winds in the Antarctic mesosphere and lower thermosphere over rothera (67°, 68°w) during 2005-2021 in meteor radar observations and WACCM-X. *Journal of Geophysical Research: Atmospheres*, *129*(4), e2023JD039789. https://doi.org/10.1029/2023JD039789

Richards, P. G., Fennelly, J. A., & Torr, D. G. (1994). EUVAC: A solar EUV flux model for aeronomic calculations. *Journal of Geophysical Research*, *99*(A5), 8981–8992. https://doi.org/10.1029/94JA00518

Richmond, A. D. (1995). Ionospheric electrodynamics using magnetic apex coordinates. *Journal of Geomagnetism and Geoelectricity*, *47*(2), 191–212. https://doi.org/10.5636/jgg.47.191

Richter, J. H., Sassi, F., & Garcia, R. R. (2010). Toward a physically based gravity wave source parameterization in a general circulation model. *Journal of the Atmospheric Sciences*, *67*(1), 136–156. https://doi.org/10.1175/2009JAS3112.1

Sato, K., Tanteno, S., Watanabe, S., & Kawatani, Y. (2012). Gravity wave characteristics in the southern hemisphere revealed by a high-resolution middle-atmosphere general circulation model. *Journal of the Atmospheric Sciences*, *69*, 1378–1396. https://doi.org/10.1175/JAS-D-11-0101.1

Sato, K., & Yoshiki, M. (2008). Gravity wave generation around the polar vortex in the stratosphere revealed by 3-hourly radiosonde observations at Syowa Station. *Journal of the Atmospheric Sciences*, *65*(12), 3719–3735. https://doi.org/10.1175/2008JAS2539.1

Senf, F., & Achatz, U. (2011). On the impact of middle-atmosphere thermal tides on the propagation and dissipation of gravity waves. *Journal of Geophysical Research*, *116*(D24), D24110. https://doi.org/10.1029/2011JD015794

Smith, A. K. (2012). Global dynamics of the MLT. *Surveys in Geophysics*, *33*(6), 1177–1230. https://doi.org/10.1007/s10712-012-9196-9

Vadas, S. L. (2007). Horizontal and vertical propagation and dissipation of gravity waves in the thermosphere from lower atmospheric and thermospheric sources. *Journal of Geophysical Research*, *112*(A6), A06305. https://doi.org/10.1029/2006JA011845

Vadas, S. L. (2013). Compressible f-plane solutions to body forces, heatings, and coolings, and application to the primary and secondary gravity waves generated by a deep convective plume. *Journal of Geophysical Research: Space Physics*, *118*(5), 2377–2397. https://doi.org/10.1002/jgra.50163

Vadas, S. L., & Azeem, I. (2021). Concentric secondary gravity waves in the thermosphere and ionosphere over the continental United States on 25–26 March 2015 from deep convection. *Journal of Geophysical Research: Space Physics*, *126*(2), e2020JA028275. https://doi.org/10.1029/2020JA028275

Vadas, S. L., & Becker, E. (2019). Numerical modeling of the generation of tertiary gravity waves in the mesosphere and thermosphere during strong mountain wave events over the Southern Andes. *Journal of Geophysical Research: Space Physics*, *124*(9), 7687–7718. https://doi.org/10.1029/2019JA026694

Vadas, S. L., Becker, E., Bossert, K., Baumgarten, G., Hoffmann, L., & Harvey, V. L. (2023). Secondary gravity waves from the stratospheric polar vortex over ALOMAR observatory on 12-14 January 2016: Observations and modeling. *Journal of Geophysical Research: Atmospheres*, *128*(2), e2022JD036985. https://doi.org/10.1029/2022JD036985

Vadas, S. L., Becker, E., Bossert, K., Hozumi, Y., Stober, G., Harvey, V. L., et al. (2024). The role of the polar vortex jet in the generation of primary and higher-order gravity waves in the stratosphere, mesosphere and thermosphere during 11-14 January 2016. *Journal of Geophysical Research: Space Physics*, *129*(9), e2024JA032521. https://doi.org/10.1029/2024JA032521

Vadas, S. L., & Fritts, D. C. (2002). The importance of spatial variability in the generation of secondary gravity waves from local body forces. *Geophysical Research Letters*, *29*(20), 1984. https://doi.org/10.1029/2002GL015574

Vadas, S. L., Fritts, D. C., & Alexander, M. J. (2003). Mechanisms for the generation of secondary waves in wave breaking regions. *Journal of the Atmospheric Sciences*, *60*(1), 194–214. https://doi.org/10.1175/1520-0469(2003)060<0194:MFTGOS>2.0.CO;2

Vadas, S. L., & Nicolls, M. J. (2012). The phases and amplitudes of gravity waves propagating and dissipating in the thermosphere: Theory. *Journal of Geophysical Research*, *117*, A05322. https://doi.org/10.1029/2011JA017426

Vadas, S. L., Themens, D., Huba, J. D., Becker, E., Bossert, K., Goncharenko, L. P., et al. (2025). Higher-order gravity waves and traveling ionospheric disturbances from the polar vortex jet on 11-15 January 2016: Modeling with HIAMCM-SAMI3 and comparison with observations in the thermosphere and ionosphere. *Journal of Geophysical Research: Space Physics*, *130*(1), e2024JA033040. https://doi.org/10.1029/2024JA033040

Vadas, S. L., Zhao, J., Chu, X., & Becker, E. (2018). The excitation of secondary gravity waves from local body forces: Theory and observation. *Journal of Geophysical Research: Atmospheres*, *123*(17), 9296–9325. https://doi.org/10.1029/2017JD027970

Watanabe, S., Sato, K., & Takahashi, M. (2006). A general circulation model study of the orographic gravity waves over Antarctica excited by katabatic winds. *Journal of Geophysical Research*, *111*, D18104. https://doi.org/10.1029/2005JD006851

Weimer, D. R. (2005). Improved ionospheric electrodynamic models and application to calculating joule heating rates. *Journal of Geophysical Research*, *110*, A10A05306. https://doi.org/10.1029/2004JA010884